machines

Article

Robust Cooperative Control for Heavy-Haul Group Trains via Tube-MPC Considering Wheel–Rail Adhesion

Huazhen Yu [1,*], Wen Zhao [1], Andrea D'Ariano [2], Ruifei An [1], Peng Xu [3] and Anzheng Lai [4]

1 School of Automation and Electrical Engineering, Lanzhou Jiaotong University, Lanzhou 730070, China
2 Department of Civil, Computer Science and Aeronautical Technologies Engineering, Roma Tre University, 00146 Rome, Italy
3 Signal and Communication Research Institute, China Academy of Railway Sciences, Beijing 100081, China
4 School of Automation and Intelligence, Beijing Jiaotong University, Beijing 100044, China
* Correspondence: hzyu@lzjtu.edu.cn

Abstract

Heavy-haul railways are mainly located in mountainous regions, where wheel–rail adhesion is susceptible to variations in rail-surface conditions, posing challenges to the cooperative operation control of heavy-haul group trains (HHGTs). This paper develops an adhesion-dependent Tube-based model predictive control (Tube-MPC) method for HHGTs by incorporating adhesion conditions into disturbance set construction, robust error Tube design, and nominal constraint tightening. A control-oriented longitudinal dynamics model retaining position-dependent gradient resistance is established to describe the motion of heavy-haul trains. Adhesion-dependent limits on traction and braking forces are imposed as input constraints, while adhesion uncertainty is modeled as a bounded equivalent acceleration disturbance arising from adhesion-induced force mismatch. An ancillary feedback controller is employed to regulate actual-nominal state deviations and ensure robust constraint satisfaction. Simulations are conducted using parameters of approximately 5000 t heavy-haul trains and a real railway gradient profile under dry, wet, and rainy or snowy rail-surface conditions. The results demonstrate that, when the actual disturbance remains within the design bound, the trajectories of all following trains remain within the error Tube. Compared with PID and standard MPC, the proposed approach improves speed coordination and spacing regulation, indicating its effectiveness for the cooperative operation of HHGTs under complex wheel–rail adhesion conditions.

Keywords: heavy-haul group trains; wheel-rail adhesion; Tube-based model predictive control; robust constraint tightening; cooperative control

Academic Editors: Yougang Sun, Hongliang Pan, Haiyan Qiang and Daofang Chang

Received: 1 September 2026
Revised: 25 September 2026
Accepted: 28 September 2026
Published: 29 September 2026

1. Introduction

With the continuous growth of heavy-haul railway transportation demand in China, existing railway lines are facing higher requirements in terms of line capacity, operational flexibility, and safety. Train group operation, supported by train-to-train communication and cooperative control technologies, enables logical virtual coupling among trains and helps overcome the limitations of traditional mechanical coupling. Without large-scale reconstruction of existing infrastructure, this operation mode can reduce train-following intervals and improve line utilization. It has therefore become an important direction for the intelligent development of heavy-haul railways.

Compared with passenger trains, heavy-haul trains are characterized by long formations, large mass, high traction and braking demands, and strong longitudinal dynamic coupling. Their operation states are strongly affected by track gradients, running resistance, and wheel–rail adhesion conditions. When multiple heavy-haul trains operate as a group with short inter-train distances, external disturbances not only reduce the speed-tracking accuracy of train units, but also affect inter-train spacing regulation. In particular, under wet, rainy or snowy rail-surface conditions, variations in the wheel–rail adhesion coefficient may reduce the collaborative control performance of trains. Therefore, achieving safe, stable, and robust cooperative control of heavy-haul group trains (HHGTs) under different wheel–rail adhesion conditions remains an important issue in intelligent heavy-haul railway operation.

Extensive studies have been conducted on train group operation and cooperative control from the perspectives of operation modes, key technologies, and application prospects [1,2]. Representative approaches include conventional feedback control, consensus-based control, sliding-mode control, observer-based control, reinforcement learning control, and model predictive control (MPC) [3,4]. Proportional integral derivative (PID) control [5,6] generates traction or braking commands based on state deviations between trains, and it is straightforward to implement but cannot explicitly handle constraints. Consensus-based control [3] coordinates train speed and spacing via local information exchange and offers good distributed scalability, yet its capability to handle complex operational constraints is limited. Sliding-mode control [7,8] improves robustness against matched disturbances and model uncertainties, but may require additional mechanisms to mitigate chattering and enforce hard safety constraints. Observer-based control [8,9] enhances disturbance rejection by estimating unmeasurable states or unknown disturbances online and compensating for their effects through feedback. Reinforcement learning-based control [10,11] uses operation data or online interactions to approximate unknown nonlinear dynamics and optimize control policies; in particular, multilayer neuroadaptive reinforcement learning based on the Actor–Critic mechanism provides strong nonlinear approximation and adaptation when an accurate system model is unavailable. Nevertheless, rigorous analytical verification of its closed-loop safety and constraint satisfaction remains challenging. In contrast, MPC-based methods [12–24] can predict future states within a receding-horizon optimization framework and explicitly incorporate state constraints, control-input constraints, and safe inter-train spacing constraints. They have therefore received considerable attention in train operation control and virtual coupling.

Centralized MPC has been applied to train trajectory tracking and cooperative operation control [12,13]. As the number of trains in a group increases, the computational complexity and communication burden associated with centralized optimization also increase. Distributed MPC has consequently been applied to metro trains, heavy-haul trains, and virtually coupled trains [14–17], improving control performance through local optimization and information exchange among adjacent trains. Hierarchical MPC separates trajectory planning from tracking control to improve the computational efficiency of complex train systems [18–20], whereas event-triggered MPC reduces the system operating burden by decreasing the number of communication events or the optimization update frequency [21]. However, model mismatch and external disturbances may cause actual train states to deviate from nominal predictions, thereby degrading control performance and potentially causing violations of state or input constraints. Robust MPC explicitly accounts for bounded uncertainties in the prediction and optimization process, whereas Tube-MPC further employs an ancillary feedback controller, a robust positively invariant error set, and constraint tightening to bound state deviations and preserve robust constraint satisfaction [22–25].

In practical operation, the cooperative control of group trains may be affected by communication delays, packet losses, braking delays, positioning errors, running resistance, and environmental variations [26–31]. Regarding wheel–rail adhesion control, Uyulan et al. [32] proposed a re-adhesion control method to mitigate wheel slide following abrupt changes in the adhesion coefficient. The method adjusts traction motor torque in real time and mainly relies on feedback information such as wheelset rotational speed or creep state. Hauck et al. [33] proposed a map-based MPC method that adjusts traction and braking commands in advance according to weather and tunnel-environment information to reduce the risk of wheel spin or wheel slide. These studies provide an important foundation for train control under different adhesion conditions. However, they mainly focus on single-train operation, wheelset-level re-adhesion control, or control based on known or predictable adhesion information. The influence of wheel–rail adhesion on group-level speed coordination, spacing regulation, and constraint satisfaction in HHGTs have not yet been sufficiently investigated. More specifically, how wheel–rail adhesion should be incorporated into the input constraints and how adhesion uncertainty should be considered in the robustness-margin construction, particularly when traction or braking commands approach the adhesion saturation boundary, remain insufficiently addressed.

To further clarify the differences between the present study and existing MPC-based train-control studies, Table 1 compares their research objects and the principal factors considered.

Table 1. Comparison with representative MPC-based studies relevant to the present work.

Reference	Control Framework	HHGTs	Modeling of Gradient Resistance	Modeling of Wheel–Rail Adhesion Effects
[13]	Nonlinear MPC	No	No	No
[16]	Improved MPC	Yes	Yes	No
[22]	Tube-MPC	No	No	No
[23]	Robust MPC	No	No	No
[24]	Tube-MPC	No	No	No
[25]	Dual-mode RMPC	No	No	No
[33]	Map-based MPC	No	No	Predictive traction and braking adjustment
This study	Adhesion-dependent Tube-MPC	Yes	Yes	Adhesion-dependent input constraints and robustness-margin construction

As shown in Table 1, existing MPC-based train-control studies have mainly focused on trajectory tracking, spacing regulation, communication constraints, or bounded disturbances, while wheel–rail adhesion has received limited attention in the cooperative control of HHGTs. Although some studies have considered adhesion-related traction or braking adjustments, the influence of adhesion conditions on both control feasibility and robustness design has not been systematically addressed. For heavy-haul trains, the available wheel–rail adhesion determines the admissible traction and braking capability, whereas adhesion uncertainty may introduce deviations between the actual train dynamics and the nominal prediction model. Therefore, considering adhesion only through fixed input limits cannot fully characterize the cooperative operation performance under varying adhesion conditions. Different from existing studies, the novelty of this work lies in developing an adhesion-dependent Tube-MPC framework, where wheel–rail adhesion effects are incorporated into both the input constraints formulation and the robustness-margin construction.

Based on the above analysis, this study focuses on the cooperative control of HHGTs under complex wheel–rail adhesion conditions, and proposes a Tube-MPC cooperative control method that considers multiple operational constraints and wheel–rail adhesion. The main contributions are summarized as follows:

(1) A control-oriented longitudinal dynamics model is formulated for heavy-haul trains by considering the position-dependent gradient resistance. The gradient resistance of vehicles is evaluated according to their actual positions and then aggregated at the train level, thereby retaining the influence of varying gradients and providing a suitable basis for cooperative control design.

(2) An adhesion-dependent Tube-MPC method is developed by coupling wheel–rail adhesion conditions with physical input constraints and robustness-margin construction. Adhesion-dependent traction and braking limits are formulated as input constraints, while adhesion uncertainty is represented through the traction or braking-force mismatch induced by adhesion saturation, and the resulting equivalent acceleration disturbance is incorporated into the robust error Tube construction and nominal constraint tightening.

(3) Simulations are conducted using parameters of a 5000 t heavy-haul train and actual line data under multiple rail-surface conditions, including dry, wet, and rainy or snowy. Disturbance bound tests verify the finite-horizon error bounds used in the Tube construction, while comparisons with PID and standard MPC are conducted to evaluate speed coordination and spacing maintenance performance.

The rest of this paper is organized as follows. Section 2 presents the mathematical formulation of the studied problem. Section 3 presents the adhesion-dependent cooperative controller within the Tube-MPC framework. Section 4 presents numerical simulations and comparative analyses. In Section 5, conclusions are given.

2. Problem Formulation

A train longitudinal dynamics model is utilized to investigate the tracking control of heavy-haul trains under real-world railway, where a "leader-follower" platoon operation scheme is implemented, as shown in Figure 1. In HHGTs, the first train acts as the leader train, which is responsible for tracking the desired trajectory. The remaining $n-1$ trains are regarded as following trains and are labeled from Train 2 to Train n.

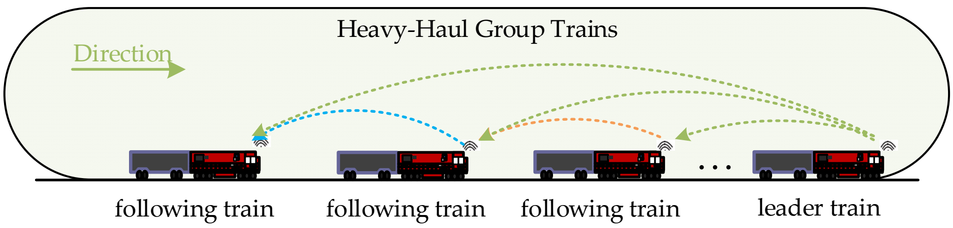

Figure 1. Heavy-haul train operation.

2.1. Train Dynamics Model

A heavy-haul train considered in this study consists of one locomotive and a series of wagons. The locomotive provides the effort required for train operation, whereas the wagons are used to transport freight. Each vehicle, whether the locomotive or a wagon, is treated as a mass point. Accordingly, the longitudinal dynamics of the heavy-haul train can be formulated as follows [16]:

$$\begin{cases} \dot{v}_{i,j} = \dfrac{1}{m_{i,j}}\left(f_{i,j}^t - f_{i,j}^e - f_{i,j}^a - f_{i,j}^c - r_{i,j} - g_{i,j}\right), (j=1) \\ \dot{v}_{i,j} = \dfrac{1}{m_{i,j}}\left(-f_{i,j}^a + f_{i,j-1}^c - f_{i,j}^c - r_{i,j} - g_{i,j}\right), (j=2,3,\cdots,n) \\ \dot{s}_{i,j} = v_{i,j}, \left(j=1,2,\cdots,n\right) \end{cases} \tag{1}$$

where $i \in \{1,\cdots,N\}$ denotes the train index, and $j \in \{1,\cdots,n\}$ denotes the vehicle index within the ith train, here, N is the total number of trains in the group, and n is the number of vehicles in each train; $m_{i,j}$, $v_{i,j}$, and $s_{i,j}$ denote the mass, speed, and position of the jth vehicle in the ith train, respectively. Here, the unit of $m_{i,j}$ is kg, the unit of $v_{i,j}$ is m/s, and the unit of $s_{i,j}$ is m; $f_{i,j}^t$ and $f_{i,j}^e$ denote the traction force and electric braking force acting on the locomotive, while $f_{i,j}^a$ denotes pneumatic braking force acting on the jth vehicle; $r_{i,j}$ and $g_{i,j}$ denote the basic resistance and additional resistance, respectively; $f_{i,j-1}^c$ and $f_{i,j}^c$ represent the front and rear coupler forces acting on the jth vehicle, respectively. All force-related terms in Equation (1) are expressed in N. The front coupler force of the first vehicle and the rear coupler force of the last vehicle are both zero, i.e., $f_{i,0}^c = 0$ and $f_{i,n}^c = 0$.

The basic resistance [17] can be expressed as follows:

$$r_{i,j} = c_0 + c_1 v_{i,j} + c_2 v_{i,j}^2 \tag{2}$$

where c_0, c_1, c_2 represent the basic resistance coefficients, their units are N, N/(m/s), and N/(m/s)^2.

The additional resistance [17] includes the gradient resistance and the curve resistance, which can be formulated as

$$g_{i,j} = \left(1000\sin\theta + \frac{600}{R}\right) m_{i,j} g \times 10^{-3} \tag{3}$$

where θ denotes the track gradient angle, R represents the radius of the track curve (m), and $g = 9.81\,\text{m/s}^2$ is the gravitational acceleration.

By summing the vehicle-level longitudinal dynamics in Equation (1), the coupler forces cancel pairwise, while the aggregate traction or braking force, running resistance, and position-dependent gradient resistance are retained. Consequently, the dynamics of the heavy-haul train can be represented by the following equivalent model:

$$\begin{cases} \dot{v}_i = \dfrac{1}{M_i}\left(F_i - F_{r,i} - F_{g,i}\right) \\ \dot{s}_i = v_i \end{cases} \tag{4}$$

where $F_i = \sum_{j=1}^{n} F_{i,j}$, $F_{i,j} = \begin{cases} f_{i,j}^t - f_{i,j}^e - f_{i,j}^a & (j=1) \\ -f_{i,j}^a & (j=2,3,\ldots,n) \end{cases}$, $M_i = \sum_{j=1}^{n} m_{i,j}$, $F_{r,i} = \sum_{j=1}^{n} r_{i,j}$, $F_{g,i} = \sum_{j=1}^{n} g_{i,j}$.

Assumption 1 (Common-speed approximation)**.** *Under normal operation of an approximately 5000 t heavy-haul train over a track with relatively mild gradients, the relative speed differences between adjacent vehicles are assumed to be small compared with the overall train speed. Therefore, the individual vehicle speeds are approximated by a common train speed when calculating the running resistance and constructing the reduced-order train-level model, i.e.,* $v_{i,j} \approx v_i$.

The gradient resistance of each vehicle is evaluated according to its actual position along the track and then summed over the complete train. Therefore, the influence of spatially varying gradients on the longitudinal dynamics of the train is retained.

It should be emphasized that the pairwise cancelation of the coupler forces in the equivalent model does not imply that these forces vanish physically. The resulting equivalent model does not explicitly represent the dynamic distribution of coupler forces and draft-gear responses. Therefore, it is intended for train speed tracking and inter-train spacing regulation rather than detailed in-train longitudinal force analysis. This limitation is particularly relevant under severe operating conditions, such as emergency braking.

Based on the common-speed assumption, the basic resistance is linearized around the equilibrium speed v_r as follows:

$$r_{i,j} = c_0 - c_2 v_r^2 + (c_1 + 2c_2 v_r)v_i \tag{5}$$

In order to adapt to the cooperative control needs of the group trains, the practical physical control force is converted into a control variable at the pure kinematics level. Dividing both sides of the equivalent model by the total mass of the train unit M_i, and considering the external unmodeled disturbance $w_i(t)$, the linear continuous state-space equation of the group trains considering disturbances can be represented as

$$\begin{cases} \dot{v}_i = u_i^{vc} + h_i v_i + l_i + p_i + w_i \\ \dot{s}_i = v_i \end{cases} \tag{6}$$

where u_i^{vc} denotes the control input per unit mass, $h_i = -\frac{1}{M_i}(c_1 + 2c_2 v_r)$, $l_i = -\frac{1}{M_i}(c_0 - c_2 {v_r}^2)$, and $p_i = -\frac{F_{g_i}}{M_i}$. The disturbance $w_i(t)$ is represented as an equivalent acceleration disturbance directly acting on the speed dynamics and is assumed to be bounded, i.e., $w_i(t) \in \mathbb{W} = \{ w_i \in \mathbb{R} : \|w_i(t)\|_\infty \le \eta \}$, where η denotes the corresponding disturbance bound. In this study, the adhesion-induced component of $w_i(t)$ is constructed from the mismatch between the actual and nominal longitudinal traction/braking forces after wheel–rail adhesion saturation. The detailed formulation of the adhesion-saturation-induced disturbance and its bound is given in Section 2.2. Since this equivalent disturbance enters the longitudinal dynamics in the form of acceleration, it directly affects the speed and indirectly affects the position through the integration of the speed deviation.

When $M_i = M$, then $h_i = h$. Incorporating l_i into w_i, the simplified equation is obtained as $\dot{v}_i = u_i^{vc} + hv_i + p_i + w_i$.

Based on the topology structure of the group trains in Figure 2, and the leader-referenced tracking strategy, the state deviation variable in this study is defined as $x_i(t) = [\Delta s_i(t), \Delta v_i(t)]^T$, in which $\Delta s_i(t) = s_1(t) - s_i(t) - d_i(t)$ is the relative distance deviation, $\Delta v_i(t) = v_1(t) - v_i(t)$ is the speed deviation, and $d_i(t)$ is the ideal tracking distance:

$$d_i(t) = (i-1)(t_d v_1(t) + S_d + S_l) \tag{7}$$

where t_d is the fixed time headway, representing that under ideal circumstances, train unit i will travel to the original position of the preceding train $i-1$ after running for t_d seconds; S_d is the fixed spacing between adjacent train units, and S_l is the train length. Meanwhile, the state-space equation can be described as the following form:

$$\dot{x}_i(t) = A^c x_i(t) + B^c u_i^{vc}(t) + D_i^c(t) + W_i^c(t) \tag{8}$$

Using the forward Euler method to achieve discretization, the discrete state equation is derived as

$$x_i(t_{k+1}) = Ax_i(t_k) + Bu_i^{vc}(t_k) + D_i(t_k) + W_i(t_k) \tag{9}$$

where the coefficient matrices are defined as $A = \begin{pmatrix} 1 & \delta \\ 0 & 1+\delta h \end{pmatrix}$, $B = \begin{pmatrix} 0 \\ -\delta \end{pmatrix}$, $W_i(t_k) = \begin{bmatrix} 0 \\ -\delta w_i \end{bmatrix}$, and $D_i(t_k) = \begin{bmatrix} -\delta(i-1)t_d(u_1^{vc} + hv_1) \\ \delta(u_1^{vc} + p_1 - p_i) \end{bmatrix}$; δ represents the sampling interval.

The above model (9) contains an uncertain disturbance variable $w_i(t_k)$, which is difficult to be used for the state trajectory prediction of train i. Therefore, a nominal system state equation unaffected by disturbances is defined to serve as the prediction model for the subsequent Tube-MPC:

$$\bar{x}_i(t_{k+1}) = A\bar{x}_i(t_k) + B\bar{u}_i^{vc}(t_k) + D_i(t_k) \tag{10}$$

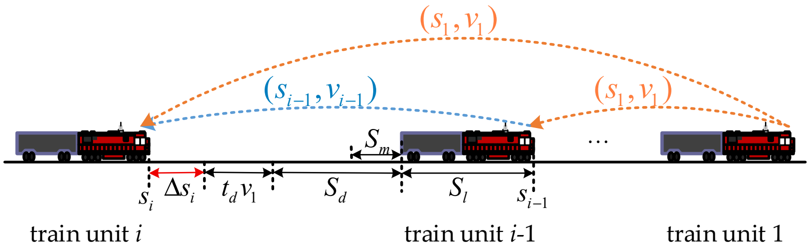

Figure 2. Topology structure of the group trains.

2.2. Wheel–Rail Adhesion Characteristics

Wheel–rail adhesion is the physical basis for locomotives and wagons to achieve guidance, running, etc. Due to the long distance of heavy-haul freight transportation and the complex operation environment, the wheel–rail adhesion state will be affected by multiple factors such as line conditions, wheel–rail contact conditions, and external environmental changes, showing nonlinear and characteristics that depend on the rail-surface condition. The adhesion characteristics of the wheel–rail rolling contact surface directly determine the performance of the traction and braking of heavy-haul trains; thus, a good wheel–rail adhesion state is an important condition to ensure the stable operation of trains. Because the wheel–rail contact surface is exposed to the open environment for a long time, its adhesion state is easily affected by the contamination of a third medium, such as rain, snow, etc. Normally, the wheel–rail adhesion coefficient under clean and dry rail-surface conditions is higher, while under rainy or snowy rail-surface conditions, the adhesion coefficient will be significantly reduced. Once the available adhesion force between the wheel and rail cannot satisfy the current traction or braking demand of the train, the originally stable wheel rolling-sliding state will quickly transform into a full sliding state, thereby leading to a serious creep/slip phenomenon.

The rail-surface adhesion coefficient μ can be described by the following empirical formula [33]:

$$\mu = ce^{-av_s} - de^{-bv_s} \tag{11}$$

where *a*, *b*, *c*, and *d* are parameters characterizing the rail-surface conditions, which are obtained by fitting experimental data under different rail conditions; v_s represents the sliding or creep speed, denoting the speed difference between the wheelset speed and the locomotive speed.

Figure 3 illustrates the adhesion characteristic curves under different rail-surface conditions. Although the adhesion curves for various rail conditions possess distinct optimal creep speeds and maximum adhesion coefficients, their overall variation trends are fundamentally consistent. Specifically, as the creep speed increases, the adhesion coefficient initially rises gradually and reaches its peak at a specific creep speed; as the creep speed continues to increase, the adhesion coefficient subsequently declines. This peak point corresponds to the maximum available wheel–rail adhesion force, and the corresponding creep speed is defined as the optimal creep speed.

The area to the left of the peak point is designated as the stable region, within which the adhesion coefficient increases with the rising creep speed. Conversely, the area to the right of the peak point represents the wheel slip or skid region, which easily manifests as wheel spin under traction conditions and as wheel slide under braking conditions. Therefore, to fully utilize the wheel–rail adhesion force and prevent adhesion instability, the locomotive control system should firmly ensure that the train operation status is maintained within the stable region.

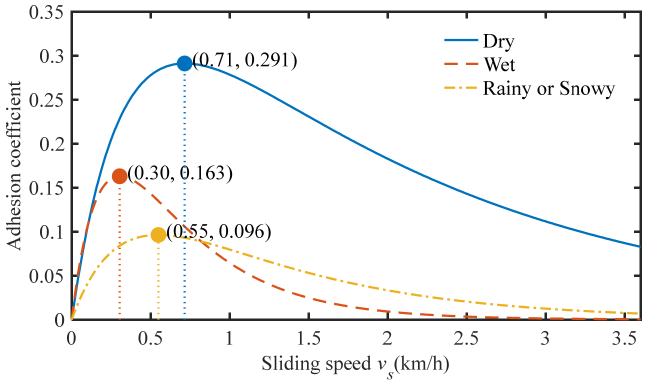

Figure 3. Adhesion characteristic curves under different rail-surface conditions.

The wheel–rail adhesion coefficient is jointly determined by the creep speed and the rail-surface conditions, directly dictating the upper bound constraint of the locomotive traction and braking forces. Regardless of whether the train operates under traction or braking conditions, the maximum available adhesion force $F_{\mu,\max}$ between the wheel and rail can be uniformly expressed as [33]:

$$F_{\mu,\max} = \mu \cdot M_{\mu} g \tag{12}$$

where M_{μ} represents the adhesive mass of the locomotive.

Taking the SS4B electric locomotive as an example, Figure 4 illustrates the comparison between the maximum adhesion force under different rail-surface conditions and the locomotive traction or braking characteristic curves. Specifically, the dashed lines represent the maximum traction or braking forces calculated based on adhesion conditions, while the solid lines denote the traction and braking characteristic curves of the SS4B locomotive [34]. As observed from the figure, the maximum adhesion force reaches its highest level under dry rail-surface conditions and consistently exceeds the traction or braking characteristic curves of the SS4B locomotive. This indicates that the existing traction or braking performance of the locomotive can be fully utilized under favorable rail conditions. However, as the rail-surface conditions degrade, the wheel–rail adhesion coefficient decreases accordingly. Consequently, the maximum adhesion force under wet, rainy or snowy rail-surface conditions drops significantly, falling below the characteristic curves of the SS4B locomotive. Therefore, to prevent wheel spin or slide phenomena during traction or braking processes, the traction and braking forces must be appropriately restricted according to the considered wheel–rail adhesion condition.

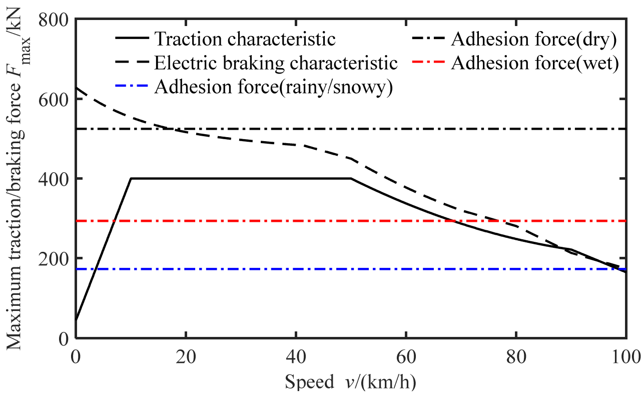

Figure 4. Comparison between maximum wheel–rail adhesion forces under different rail-surface conditions and locomotive characteristic curves.

To improve wheel–rail adhesion utilization and ensure operation stability under complex and variable track environments, the locomotive operating state should be maintained near the selected stable adhesion operating point [35]. Relative to the selected operating point, the actual adhesion coefficient μ' can be decomposed as follows:

$$\mu' = \mu_0 + \Delta\mu \tag{13}$$

where μ_0 denotes the nominal adhesion coefficient determined by the nominal creep speed and the nominal rail-surface condition, and $\Delta\mu$ represents the deviation in the actual adhesion coefficient from the nominal adhesion coefficient within the prescribed operating region.

Assumption 2 (Availability of adhesion information)**.** *An estimate of the current wheel–rail adhesion coefficient, or a conservative lower bound on the available adhesion, together with a bounded variation range within the prescribed operation region, is assumed to be available to the controller before the online optimization process.*

Remark 1. *The present study focuses on adhesion-dependent robust control under available adhesion information rather than developing a complete adhesion estimation and control system. The required adhesion information can be obtained from existing adhesion estimation approaches or prior knowledge of operation conditions. In particular, an online adhesion-estimation module based on wheelset angular speed, vehicle speed, or creepage speed measurements is beyond the scope of this study. Accordingly, the proposed controller is applicable when such adhesion information is available.*

To characterize the longitudinal acceleration mismatch caused by adhesion saturation, let $U_{\min}(\mu, v_i)$ and $U_{\max}(\mu, v_i)$ denote the adhesion and speed dependent lower and upper control-input limits, respectively, whose explicit expressions are given in Section 2.3.

To describe the effect of adhesion saturation, the saturation operator is defined as

$$\mathrm{sat}(u; U_{\min}, U_{\max}) = \min\{U_{\max}, \max(U_{\min}, u)\} \tag{14}$$

For the commanded control input u_i^{vc}, the effective acceleration input under the actual adhesion coefficient μ' is

$$u_i^{\mathrm{act}} = \mathrm{sat}\left[u_i^{vc}; U_{\min}(\mu', v_i), U_{\max}(\mu', v_i)\right] \tag{15}$$

Similarly, under the nominal adhesion coefficient μ_0, the corresponding nominal transmitted control input is

$$u_i^{0} = \mathrm{sat}\left[u_i^{vc}; U_{\min}(\mu_0, v_i), U_{\max}(\mu_0, v_i)\right] \tag{16}$$

Accordingly, the equivalent acceleration disturbance caused by wheel–rail adhesion variation is defined as

$$w_{\mu,i} = u_i^{\mathrm{act}} - u_i^{0} \tag{17}$$

Therefore, the adhesion-induced disturbance depends jointly on the commanded control input, train speed, and available adhesion condition. When the commanded control input remains within the admissible input range under both the actual and nominal adhesion conditions, $u_i^{\mathrm{act}} = u_i^{0} = u_i^{vc}$, $w_{\mu,i} = 0$. For the subsequent Tube construction, the worst-case equivalent acceleration disturbance bound is evaluated as

$$\eta_{\mu,i} = \max_{\substack{\mu' \in [\mu_{\min}, \mu_{\max}] \\ u_i^{vc}(t) \in \mathbb{U}}} \left| u_i^{\text{act}} - u_i^0 \right| \tag{18}$$

Accordingly, when only the adhesion-induced uncertainty is considered, the disturbance set is defined as

$$\mathbb{W} = \left\{ w_i \in \mathbb{R} : \left\| w_i(t) \right\|_\infty \le \eta_{\mu,i} \right\} \tag{19}$$

The robust constraint-satisfaction guarantee of the proposed method is valid only when the creep speed remains within the prescribed stable adhesion region and the equivalent acceleration uncertainty remains within the designed disturbance bound.

2.3. Constraints and Control Objectives

The control system must satisfy physical actuator constraints, track speed limit constraints, and safety spacing constraints. The admissible traction and braking inputs are jointly limited by the locomotive traction/braking characteristics and the available wheel–rail adhesion force. Considering the locomotive characteristic curves shown in Figure 4, the maximum admissible traction force is defined as

$$F_{t,\max}(\mu, v) = \min\left[F_{t,\,\text{char}}(v), \mu \cdot M_\mu g \right], \tag{20}$$

where $F_{t,\,\text{char}}$ denotes the maximum traction force provided by the locomotive traction characteristic at speed v.

Similarly, the maximum admissible braking-force magnitude is defined as

$$F_{b,\max}(\mu, v) = \min\left[F_{b,\,\text{char}}(v), \mu \cdot M_\mu g \right], \tag{21}$$

where $F_{b,\,\text{char}}$ denotes the maximum braking-force magnitude determined by the braking characteristic at speed v.

Since the control input u_i^{vc} is defined as the longitudinal control force per unit total train mass, the corresponding acceleration limits are

$$\begin{aligned} U_{\max}(\mu, v) &= \frac{1}{M_i} \min\left[F_{t,\,\text{char}}(v), \mu \cdot M_\mu g \right] \\ U_{\min}(\mu, v) &= -\frac{1}{M_i} \min\left[F_{b,\,\text{char}}(v), \mu \cdot M_\mu g \right] \end{aligned} \tag{22}$$

Therefore, the physical input constraint set is explicitly defined as

$$u_i^{vc}(t) \in \mathbb{U} \triangleq \left\{ u_i^{vc}(t) \in \mathbb{R} : U_{\min}(\mu, v) \le u_i^{vc}(t) \le U_{\max}(\mu, v) \right\} \tag{23}$$

where $U_{\max} > 0$ represents the maximum admissible traction acceleration, whereas $U_{\min} < 0$ represents the maximum admissible braking deceleration. Thus, the admissible control input is simultaneously constrained by the locomotive traction/braking capability and the available wheel–rail adhesion condition.

The train operation speed is subject to the track speed limit constraint:

$$v_i(t) \le v_{\lim}(s_i(t)) \tag{24}$$

where $v_{\lim}(s_i(t))$ is the speed limit value at position $s_i(t)$.

In the process of operation, HHGTs need to maintain a certain safe tracking distance between adjacent train units to prevent rear-end collision accidents. To ensure the safe operation of the train platoon, the dynamic minimum spacing S_{safe} between two adjacent train units must satisfy

$$\begin{aligned} S_{safe} &= S_m + \max\left(\frac{v_{i-1}^2(t)}{2U_{\min}} - \frac{v_i^2(t)}{2U_{\min}}, 0 \right) \\ s_{i-1}(t) &- s_i(t) - S_l \ge S_{safe} \end{aligned} \tag{25}$$

where S_m is the safety margin. Since $U_{\min} < 0$ represents the braking acceleration, the braking distance of train i is $\frac{-v_i^2(t)}{2U_{\min}}$.

When $v_{i-1} - v_i \geq 0$, the speed of the preceding train is higher than that of the following train. Since this relative speed condition reduces the risk of rear-end collision, only the basic safety margin is required:

$$s_{i-1}(t) - s_i(t) - S_l \geq S_m \tag{26}$$

When $v_{i-1} - v_i < 0$, the following train travels faster than the preceding train. In this case, an additional safety distance caused by the relative speed difference is considered:

$$s_{i-1}(t) - s_i(t) - S_l \geq S_m + \frac{v_{\lim}}{U_{\min}}(v_{i-1}(t) - v_i(t)) \tag{27}$$

Therefore, Equations (26) and (27) ensure that sufficient braking space is maintained between adjacent trains under different relative motion conditions. Compared with the original nonlinear braking distance constraint $S_{original} = \frac{v_i^2(t) - v_{i-1}^2(t)}{-2U_{\min}}$, the linearized braking distance term is given by $S_{linear} = \frac{2v_{\lim}(v_i - v_{i-1})}{-2U_{\min}}$, since $v_i^2 - v_{i-1}^2 = (v_i + v_{i-1})(v_i - v_{i-1})$, $-2U_{\min} > 0$ and $(v_i + v_{i-1}) \leq 2v_{\lim}$, it follows that $S_{original} \leq S_{linear}$. Therefore, the proposed linearized constraint provides an equal or larger safety margin than the original nonlinear constraint, indicating that the approximation is conservative and does not compromise the braking-distance requirement.

To express the constraints in a compact form, defining the matrices as $\mathrm{H}_1 = [1,0]$ and $\mathrm{H}_2 = [0,1]$, the following linear constraint functions are constructed:

$$\phi_1(x_i, x_{i-1}) = \mathrm{H}_1(x_i - x_{i-1}) + t_d v_1 + S_d - S_m$$

$$\phi_2(x_i, x_{i-1}) = (\mathrm{H}_1 - \frac{v_{\lim}}{U_{\min}}\mathrm{H}_2)(x_i - x_{i-1}) + t_d v_1 + S_d - S_m$$

$$\phi_3(x_i, x_{i-1}) = \mathrm{H}_2 x_i - v_1 + v_{\lim}$$

Consequently, the state constraint set of the system can be formulated as a compact convex polyhedral set $\mathbb{X}$:

$$x_i \in \mathbb{X} \triangleq \left\{ x_i \in \mathbb{R}^2 : \phi_l(x_i, x_{i-1}) \geq 0, l = 1,2,3 \right\} \tag{28}$$

In conjunction with the aforementioned constraints, the study aims to design a robust control method that optimizes the cooperative control strategy under bounded disturbances. This method ensures satisfaction of the state constraint set $\mathbb{X}$ and the input constraint set $\mathbb{U}$ over the considered finite prediction horizon under the prescribed disturbance bound, while maintaining the desired spacing and uniform operation speed for each train unit. Its mathematical description is given by

$$\begin{gathered} \lim_{k\to\infty} \|\bar{x}_i(t_k)\|_2 = 0 \\ \lim_{k\to n_p} \|x_i(t_k)\|_2 \leq \gamma(\eta) \end{gathered} \tag{29}$$

$$\begin{gathered} \lim_{k\to\infty} \|\bar{x}_i(t_k) - \bar{x}_{i-1}(t_k)\|_2 = 0 \\ \lim_{k\to n_p} \|x_i(t_k) - x_{i-1}(t_k)\|_2 \leq 2\gamma(\eta) \end{gathered} \tag{30}$$

where Equation (29) indicates that the nominal HHGT system tends toward an equilibrium state, meaning all train units operate at a uniform speed and maintain constant separation distances. Equation (30) signifies that the relative nominal state variables between adjacent train units asymptotically converge to zero. For the actual system subject to bounded disturbances, the deviation from the nominal trajectory remains bounded within the prescribed Tube, $\gamma(\eta)$ represents the upper bound of the steady-state tracking error determined by the disturbance bound η of the disturbance set $\mathbb{W}$, and n_p is the step

https://doi.org/10.3390/machines14101122

size of the prediction horizon. The detailed derivation is provided in the proof of Theorem 4.

3. Adhesion-Dependent Cooperative Controller Design

To achieve the cooperative control of HHGTs under saturation mismatch, a Tube-MPC controller is designed. First, considering that the equivalent acceleration disturbance $w_{\mu,i}$, generated by the mismatch between the actual and nominal traction/braking forces after adhesion saturation, leads to a deviation between the actual and nominal trajectories, a finite-horizon bounded error Tube $\tilde{\mathbb{X}}$ containing the worst-case state prediction error is calculated offline using an ancillary feedback controller, which is used to construct the tightened constraints. Second, by utilizing the optimal nominal state trajectory of the preceding train $i-1$ at the previous instant $\bar{X}_{i-1,o}(t_{k-1})$ and Equation (37), its current estimated nominal state trajectory $\bar{X}_{i-1,e}(t_k)$ is obtained, and simultaneously, the estimated nominal state trajectory $\bar{X}_{i,e}(\cdot\mid t_k)$ and the estimated nominal control sequence $\bar{U}_{i,e}^{vc}(\cdot\mid t_k)$ can be obtained based on the historical information of train i, to construct the objective function $J_i(\bullet)$. Next, based on the nominal system and the objective function, train i solves the Tube-MPC optimization problem under the premise of satisfying the tightened constraints, thereby obtaining the optimal nominal control sequence $\bar{U}_{i,o}^{vc}(\cdot\mid t_k)$ and the optimal nominal state trajectory, and transmits $\bar{X}_{i,o}(\cdot\mid t_k)$ to the succeeding train $i+1$. Finally, the current actual control variable $u_i^{vc}(t_k)$ is obtained through the ancillary feedback controller.

3.1. Adhesion-Dependent Tube-MPC Formulation

Due to the presence of the disturbance $w_i(t_k)$, a state prediction error $\tilde{x}_i(t_k)$ arises between the actual system and the nominal system; for the nominal MPC controller, the optimal control input of unit train i at time t_k is $\bar{u}_{i,o}^{vc}(t_k\mid t_k)$, and the actual controller is designed as

$$u_i^{vc}(t_k)=\bar{u}_{i,o}^{vc}(t_k\mid t_k)+\mathrm{K}_{\text{tube}}\tilde{x}_i(t_k) \tag{31}$$

where the feedback control gain matrix is designed as $\mathrm{K}_{\text{tube}}=\begin{pmatrix}0 & k_{tube}\end{pmatrix}$. In the design of K_{tube}, the external disturbance is assumed to directly affect the speed variable in the form of acceleration.

The finite-horizon accumulation bound is constructed primarily with respect to the speed error subsystem, because the external uncertainty considered in this study acts directly on the speed dynamics in the form of an equivalent acceleration disturbance and affects the spacing state indirectly through integration.

The detailed proofs of Theorems 1–4 are provided in Appendix A.

Theorem 1. *To ensure that the speed error subsystem is Input-to-State Stable (ISS) with respect to the bounded, the feedback gain* k_{tube} *is selected such that* $0\le 1+(h-k_{tube})\delta<1$, *i.e.,* $k_{tube}\in\left(h,\dfrac{1}{\delta}+h\right)$. *Suppose that the disturbance satisfies* $\|w_i(t)\|_\infty\le\eta$, *the initial speed prediction error satisfies* $|\tilde{v}_i(t_0)|\le\dfrac{\eta}{k_{tube}-h}$, *and the initial spacing prediction error is zero, i.e.,* $\tilde{s}_i(t_0)=0$ *.Then, for every prediction step* $k-0,1,\ldots,n_p$, $|\tilde{v}_i(t_k)|\le\dfrac{\eta}{k_{tube}-h}$, *while the spacing error, obtained by the discrete accumulation of the speed error, satisfies* $|\tilde{s}_i(t_k)|\le\dfrac{\eta\delta n_p}{k_{tube}-h}$. *Therefore, the speed error subsystem is ISS, whereas the spacing error component is bounded over the finite prediction horizon. Accordingly, the state deviation over the prediction horizon is characterized by a finite-horizon* *bounded error Tube, namely* $\tilde{x}_i(t_k)=[\tilde{s}_i(t_k),\tilde{v}_i(t_k)]^T\in\tilde{\mathbb{X}}$, $\tilde{s}_i(t)=\Delta s_i(t)-\Delta\bar{s}_i(t)$, $\tilde{v}_i(t)=\Delta v_i(t)-\Delta\bar{v}_i(t)$, *where the Tube* $\tilde{\mathbb{X}}$ *is defined as*

$$\tilde{\mathbb{X}}\triangleq\left\{\tilde{x}_i(t_k)\in\mathbb{R}^2:|\tilde{x}_i|\le\begin{pmatrix}\dfrac{\eta\delta n_p}{k_{tube}-h}\\ \dfrac{\eta}{k_{tube}-h}\end{pmatrix}\right\}\tag{32}$$

Theorem 2. *To ensure that the actual HHGTs system does not violate physical safety constraints over the considered finite prediction horizon when the actual disturbance remains within the design disturbance bound, the Pontryagin difference set theorem is utilized to strictly tighten the original non-safe boundaries inward. Because* $\tilde{u}_i^{vc}=k_{\mathrm{tube}}\tilde{v}_i(t_k)$, *the actual control input* $\bar{u}_i^{vc}$ *will not exceed the train traction and braking performance limits as long as the nominal control input* u_i^{vc} *satisfies the tightened input constraints* $\bar{\mathbb{U}}\ominus\mathrm{K}_{\mathrm{tube}}\tilde{\mathbb{X}}$:

$$\bar{\mathbb{U}}\triangleq\left\{\bar{u}_i^{vc}:U_{\min}(\mu,v)+\frac{k_{tube}\eta}{k_{tube}-h}\le\bar{u}_i^{vc}\le U_{\max}(\mu,v)-\frac{k_{tube}\eta}{k_{tube}-h}\right\}\tag{33}$$

If the nominal state variable $\bar{x}_i$ *satisfies* $\bar{x}_i\in\bar{\mathbb{X}}$, *then the actual state variable* x_i *will satisfy the constraints in Equation (28), i.e.,* $x_i\in\mathbb{X}$, *and the actual state variable* x_i *remains within the Tube* $\mathrm{T}\triangleq\bar{x}_{i,o}\oplus\tilde{\mathbb{X}}$ *[24] over the considered prediction horizon.*

$$\bar{\mathbb{X}}\triangleq\left\{\bar{x}_i:\phi_l'(\bar{x}_i,\bar{x}_{i-1})\ge 0,l=1,2,3\right\}\tag{34}$$

The corresponding tightened constraint functions are given by

$$\phi_1'(\bar{x}_i,\bar{x}_{i-1})=\mathrm{H}_1(\bar{x}_i-\bar{x}_{i-1})-\frac{2\eta\delta n_p}{k_{tube}-h}+t_dv_1+S_d-S_m$$

$$\phi_2'(\bar{x}_i,\bar{x}_{i-1})=(\mathrm{H}_1-\frac{v_{\lim}}{U_{\min}}\mathrm{H}_2)(\bar{x}_i-\bar{x}_{i-1})-\frac{2\eta\delta n_p}{k_{tube}-h}-\frac{2\eta}{k_{tube}-h}+t_dv_1+S_d-S_m$$

$$\phi_3'(\bar{x}_i,\bar{x}_{i-1})=\mathrm{H}_2\bar{x}_i-\frac{\eta}{k_{tube}-h}-v_1+v_{\lim}$$

To construct a scalar terminal controller, the known $D_i(t_k)$ is decomposed as $D_i(t_k)=\begin{bmatrix}d_{i,1}(t_k)\\ d_{i,2}(t_k)\end{bmatrix}$.

Assumption 3 (Terminal steady-cruise condition). *Over the terminal prediction interval, the leading train is assumed to operate at an approximately constant speed. Accordingly, the acceleration-related term appearing in the first component of* $D_i(t_k)$ *satisfies* $u_1^{vc}+hv_1\approx 0$, *and hence* $d_{i,1}(t)=-\delta(i-1)t_d(u_1^{vc}+hv_1)$. *Therefore, in the terminal analysis,* $D_i(t_k)$ *can be simplified to* $D_i(t_k)=\begin{bmatrix}0\\ d_{i,2}(t_k)\end{bmatrix}$.

Theorem 3. *Suppose that there exists a terminal constraint set* $\mathbb{X}_f$, $\mathbb{X}_f=\{\bar{x}_i(t_k):\bar{u}_f(t_k)\in\bar{\mathbb{U}}\}$, *and the corresponding terminal feedback controller* $\bar{u}_f(t_k)=K_f\bar{x}_i(t_k)+\dfrac{d_{i,2}(t_k)}{\delta}$, *where* $\mathrm{K}_f=-(R+\mathrm{B}^{\mathrm{T}}\mathrm{PB})^{-1}\mathrm{B}^{\mathrm{T}}\mathrm{PA}$; *if the Tube-MPC optimization problem (39) admits a feasible solution satisfying all the constraints at time* $t_{k-1}(k>1)$ *then the optimization problem also admits a feasible solution at time* t_k.

Theorem 4. *If the group train system satisfies the following stability conditions,*

$$\begin{aligned}&Q+A^TPA-A^TPB(R+B^TPB)^{-1}B^TPA-P<0\\ &F+A^TPA-2A^TPB(R+B^TPB)^{-1}B^TPA-P<0\end{aligned}\tag{35}$$

then the nominal closed-loop HHGT system is asymptotically stable and the nominal cooperative states converge to their equilibrium values. In the presence of bounded adhesion-induced disturbances, the speed error subsystem is ISS, and the actual state remains within a disturbance-dependent neighborhood of the nominal trajectory over the considered prediction horizon.

To obtain the nominal state trajectory at the current instant for constructing the group train Tube-MPC optimization problem, the current control behavior and state trajectory are estimated based on the received historical state information and the terminal feedback controller. The specific method is as follows:

$$\begin{aligned} &\bar{U}_{i,e}^{vc}(\cdot\mid t_k)=\left\{\bar{u}_{i,e}^{vc}(t_k\mid t_k),\bar{u}_{i,e}^{vc}(t_{k+1}\mid t_k),\ldots,\bar{u}_{i,e}^{vc}(t_{k+n_p-1}\mid t_k)\right\}^T \\ &\bar{u}_{i,e}^{vc}(t_{k+m}\mid t_k)=\begin{cases}\bar{u}_{i,o}^{vc}(t_{k+m+1}\mid t_{k-1}) & m=0,1,\ldots,n_p-2\\ K_f\bar{x}_i(t_{k+n_p-1}\mid t_k)+\dfrac{d_{i,2}(t_k)}{\delta} & m=n_p-1\end{cases}\end{aligned} \tag{36}$$

$$\begin{aligned} &\bar{X}_{i,e}(\cdot\mid t_k)=\left\{\bar{x}_{i,e}(t_k\mid t_k),\bar{x}_{i,e}(t_{k+1}\mid t_k),\ldots,\bar{x}_{i,e}(t_{k+n_p}\mid t_k)\right\}^T \\ &\bar{x}_{i,e}(t_{k+m}\mid t_k)=\begin{cases}\bar{x}_{i,o}(t_{k+m+1}\mid t_{k-1}) & m=0,1,\ldots n_p-1\\ A\bar{x}_{i,e}(t_{k+n_p-1}\mid t_k)+B\bar{u}_{i,e}^{vc}(t_{k+n_p-1}\mid t_k)+D_i(t_k) & m=n_p\end{cases}\end{aligned} \tag{37}$$

where the $\bar{U}_{i,e}^{vc}(\cdot\mid t_k)$ and $\bar{X}_{i,e}(\cdot\mid t_k)$ denote the estimated nominal control sequence and estimated nominal state trajectory of train i at time step k, respectively; $\bar{u}_{i,e}^{vc}(t_{k+m}\mid t_k)$ and $\bar{x}_{i,e}(t_{k+m}\mid t_k)$ represent the estimated nominal control input and estimated nominal state of train i at the future m-th step at time step t_k, respectively; $\bar{u}_{i,o}^{vc}(t_{k+m+1}\mid t_{k-1})$ and $\bar{x}_{i,o}(t_{k+m+1}\mid t_{k-1})$ denote the optimal nominal control input and optimal nominal state at the future (m + 1)-th step obtained by train i solving the optimization problem at time step t_{k-1}, respectively.

Since the nominal state trajectory of the preceding train $i-1$ estimated based on Equation (37) may deviate from its actual trajectory, the objective function $J_i(\bullet)$ of train i is designed to suppress this estimation error and achieve the cooperative operation goal as follows:

$$\begin{aligned} &J_i(\bar{x}_i(t_k),\bar{u}_i^{vc}(t_k),\bar{x}_{i-1,e}(t_k))=\sum_{m=0}^{n_p-1}L_i(\bar{x}_i(t_{k+m}\mid t_k),\bar{u}_i^{vc}(t_{k+m}\mid t_k),\bar{x}_{i-1,e}(t_{k+m}\mid t_k))+G_i(\bar{x}_i(t_{k+n_p}),\bar{x}_{i-1,e}(t_{k+n_p}))\\ &s.t.\\ &L_i(\bar{x}_i(t),\bar{u}_i^{vc}(t),\bar{x}_{i-1,e}(t))=\left\|Q\bar{x}_i(t)\right\|_2+\left\|F(\bar{x}_i(t)-\bar{x}_{i-1,e}(t))\right\|_2+\left\|R\bar{u}_i^{vc}(t)\right\|_2\\ &G_i(\bar{x}_i(t+T_p),\bar{x}_{i-1,e}(t+T_p))=\left\|P\bar{x}_i(t+T_p)\right\|_2+\left\|P(\bar{x}_i(t+T_p)-\bar{x}_{i-1,e}(t+T_p))\right\|_2\end{aligned} \tag{38}$$

where L_i is the stage cost function to achieve precise state tracking and consensus of the train platoon, G_i is the terminal cost function to ensure the asymptotic stability at the prediction horizon terminal, T_p is the prediction horizon, and Q,F,P,R are the weight coefficient matrices.

3.2. Cooperative Control Algorithm

Combining the Tube set $\tilde{\mathbb{X}}$, the nominal state trajectory estimation method for HHGTs, the Tube-MPC optimization problem is constructed as follows:

$$\begin{aligned} &\min_{\bar{u}_i^{vc}(\cdot\mid t_k)} J_i(\bar{x}_i(t_k),\bar{u}_i^{vc}(t_k),\bar{x}_{i-1,e}(t_k))\\ &s.t.\\ &\bar{x}_i(t_{k+1+m}\mid t_k)=A\bar{x}_i(t_{k+m}\mid t_k)+B\bar{u}_i(t_{k+m}\mid t_k)+D_i(t_{k+m}\mid t_k)\\ &x_i(t_k)\in\bar{x}_i(t_k\mid t_k)\oplus\tilde{\mathbb{X}}\\ &\bar{x}_i(t_{k+m}\mid t_k)\in\bar{\mathbb{X}}\\ &\bar{u}_i^{vc}(t_{k+m}\mid t_k)\in\bar{\mathbb{U}}\\ &\bar{x}_i(t_{k+n_p}\mid t_k)\in\mathbb{X}_f\end{aligned} \tag{39}$$

The optimization problem is formulated as a second-order cone programming (SOCP) problem in YALMIP and solved by the MOSEK solver, all numerical tolerances and stopping criteria are kept at the default settings. For the above optimization problem, the modified constraint sets of the state and control variables are $\bar{\mathbb{X}} \triangleq \mathbb{X} \ominus \tilde{\mathbb{X}}$ and $\bar{\mathbb{U}} \triangleq \mathbb{U} \ominus K_{tube}\tilde{\mathbb{X}}$, and $\oplus$ and $\ominus$ denote the Minkowski sum and difference, respectively. Specifically, the procedure of the cooperative control algorithm for HHGTs based on Tube-MPC is presented in Algorithm 1.

Algorithm 1: Cooperative Control Algorithm.

Controller Setup:

1. Design the Tube feedback control gain matrix $\mathrm{K}_{\mathrm{tube}}$ according to the disturbance bound η and the sampling step size δ,and compute the Tube $\tilde{\mathbb{X}}$;

2. Tighten the state constraints and input constraints using the Pontryagin set difference theorem according to Equations (33) and (34) to obtain $\bar{\mathbb{X}}$ and $\bar{\mathbb{U}}$;

3. Select the weight coefficient matrices Q, R, P, compute the terminal feedback gain K_f, and construct the terminal constraint set $\mathbb{X}_f$;

Receding-Horizon Control:

1. Initialization: $t_k = t_0$, obtain the actual states $x_i(t_0)$ of all virtual coupling trains (or unit trains), and set the initial nominal states $\bar{x}_i(t_0) = x_i(t_0)$;

2. **for** $i = 1$ **to** N **do**

3. Receive the optimal nominal state trajectory $\bar{X}_{i-1,o}(\cdot \mid t_{k-1})$ of the preceding train $i-1$ from the previous time step, and estimate its current nominal state trajectory $\bar{X}_{i,e}(\cdot \mid t_k)$

4. Solve the Tube-MPC optimization problem (39) based on the tightened constraint sets $\bar{\mathbb{X}}$ and $\bar{\mathbb{U}}$;

5. Obtain the optimal nominal control sequence $\bar{U}_{i,o}^{vc}(\cdot \mid t_k)$ and optimal nominal state trajectory $\bar{X}_{i,o}(\cdot \mid t_k)$ for train i, and send the state trajectory to the following train $i+1$;

6. Measure the actual state $x_i(t_k)$ and calculate the prediction error $\tilde{x}_i(t_k) = x_i(t_k) - \bar{x}_i(t_k)$;

7. Execute the actual control law $u_i^{vc}(t_k) = \bar{u}_{i,o}^{vc}(t_k \mid t_k) + \mathrm{K}_{\mathrm{tube}}\tilde{x}_i(t_k)$, and apply it to the actual system;

8. Recursively deduce the nominal state $\bar{x}_i(t_{k+1})$ of the next time step based on the nominal model (10);

9. **end for**

10. Time step $t_k = t_{k+1}$; if the total simulation duration is reached, terminate; otherwise, return to step 2.

4. Simulation Verification

4.1. Parameter Settings

To validate the effectiveness of the proposed adhesion-dependent cooperative control method for HHGTs, simulations are carried out using heavy-haul train parameters and real-world railway data. The train group consists of one leader train and three following trains, with each train having a mass of approximately 5000 t. The railway line contains continuously varying gradients ranging from −4‰ to 4‰, as shown in Figure 5. To evaluate the control performance under different adhesion conditions, three representative wheel-surface adhesion scenarios, namely dry, wet, and rainy or snowy, are considered. The simulations focus on normal cooperative operation; while emergency braking and other extreme scenarios that may induce excessive intra-train longitudinal forces are beyond the scope of the study. The main simulation parameters and disturbance bounds are summarized in Table 2. For each rail-surface condition, the peak adhesion coefficient obtained from the corresponding adhesion characteristic curve is employed as the nominal adhesion coefficient μ_0 according to the adhesion characteristic parameters listed in Table 3. The adhesion uncertainty range is set as $[0.8\mu_0, \mu_0]$ based on Ref. [36]. The adhesion-induced disturbance bound is then evaluated using Equation (19) by considering the admissible ranges of the commanded traction/braking force, train speed, and adhesion coefficient. Therefore, the resulting disturbance bound reflects the worst-case acceleration mismatch caused by adhesion saturation. In addition, the bounded disturbance induced by adhesion uncertainty is modeled as a bounded acceleration disturbance, with $\|w_i(t)\|_\infty \le \eta$. Simulations are performed in MATLAB R2025b on a 64-bit Windows 10 computer equipped with a 3.6 GHz Intel i7 CPU and 16 GB of RAM.

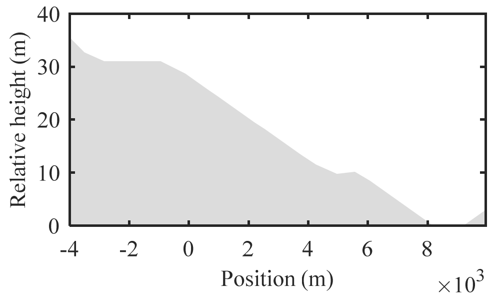

Figure 5. Track gradient data.

Table 2. Simulation parameters.

Parameter	Value	Parameter	Value
M_i / kg	5584 $\times 10^3$	k_{tube}	1
S_l / m	686.4	c_0 / N	0.9163
S_m / m	110	c_1 /N $\cdot$ (m/s)$^{-1}$	0.01721
S_d / m	800	c_2 /N $\cdot$ (m/s)$^{-2}$	0.001614
T_p / s	20	Q	$diag\{0.5, 0.5\}$
δ / s	0.5	F	$diag\{0.5, 0.5\}$
η_{dry} / (m/s^2)	0.0188	P	$diag\{4, 4\}$
η_{wet} / (m/s^2)	0.0105	R	50
η_{snow} / (m/s^2)	0.0062	u_i^{vc} / (m/s^2)	[−0.1,0.1]

When adhesion saturation is inactive, $u_i^{\text{act}} = u_i^0$ and $w_{\mu,i} = 0$; when saturation occurs, the resulting disturbance $w_{\mu,i} = u_i^{\text{act}} - u_i^0$ is bounded by the corresponding η.

Table 3. Parameters of the adhesion characteristic curves adopted from Ref. [33].

Rail-Surface Condition	*a*	*b*	*c*	*d*
Dry	0.5	3	0.5	0.5
Wet	2	5	0.5	0.5
Rainy or Snowy	1	3	0.25	0.25

4.2. Control Performance Under Different Actual Disturbance Levels

To investigate the robustness of the proposed controller against disturbance bound mismatch, the design disturbance bound is set as η. The actual disturbance bounds are selected as η and 1.5η, representing matched and mismatched disturbance conditions, respectively. The η case evaluates the control performance within the predefined disturbance range, whereas the 1.5η case evaluates the robustness under disturbance bound mismatch. The simulations are conducted under dry, wet, rainy or snowy adhesion conditions. The initial speed of HHGTs is set to 68 km/h, the initial speed and spacing deviations in the following trains are set to $\Delta v_i = -0.5\text{m/s}$ and $\Delta s_i = 5\text{m}$ ($i = 2,3,4$), relative to the leader train. Figures 6–8 show the error Tubes, actual and nominal operation trajectories of the following trains under different rail-surface conditions.

When the actual disturbance increases to 1.5η, the disturbance exceeds the assumed range used in controller design. To quantitatively evaluate the robustness against this disturbance bound mismatch, the Tube violation rate and the maximum Tube ratio are calculated for both speed and spacing states. The Tube violation rate represents the proportion of steady-state samples violating the Tube bounds, whereas the maximum Tube ratio represents the maximum normalized deviation relative to the corresponding Tube bound. A maximum Tube ratio is greater than 1 indicates that a Tube violation occurs. The statistical results of the above metrics are given in Table 4.

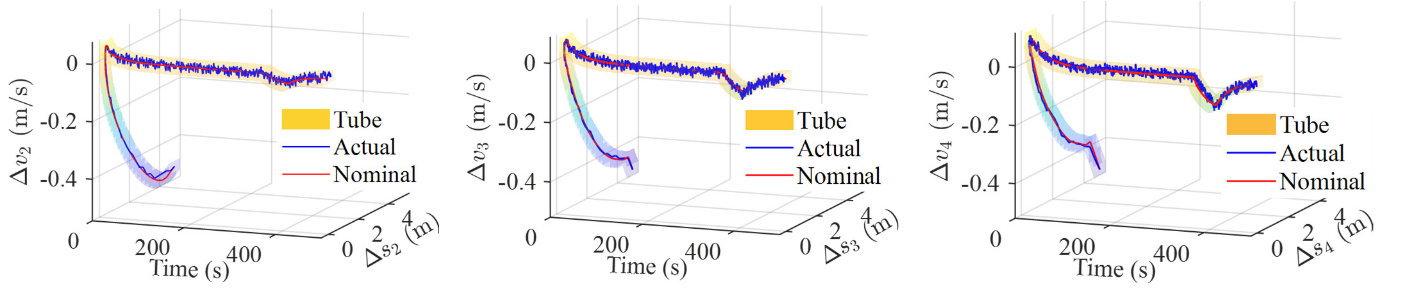

(**a**) Under the actual disturbance bound of η

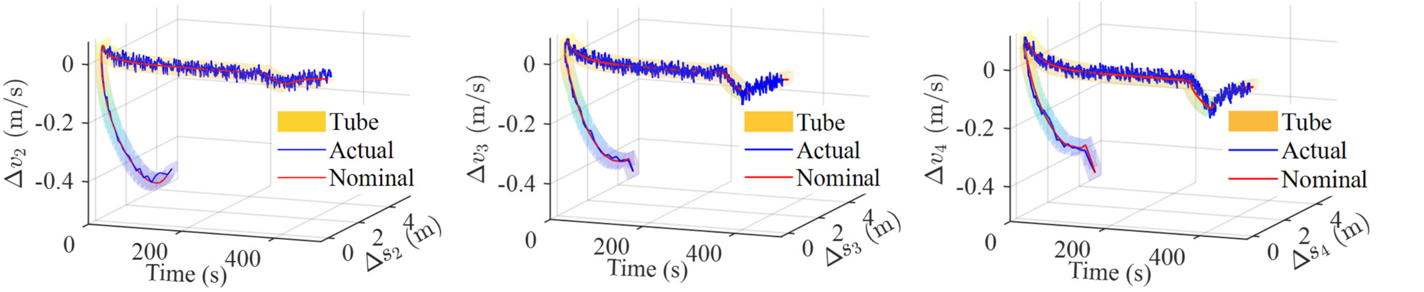

(**b**) Under the actual disturbance bound of 1.5η

Figure 6. Actual and nominal operation trajectories relative to the error Tube under dry rail-surface conditions.

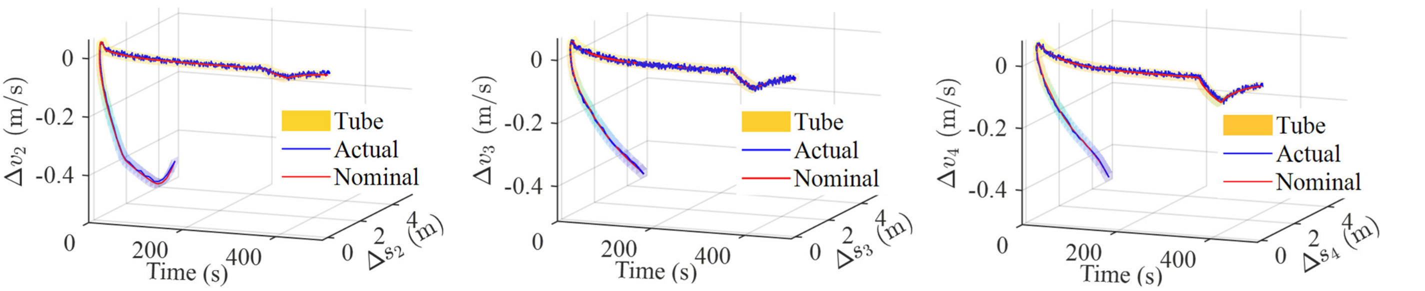

(**a**) Under the actual disturbance bound of η

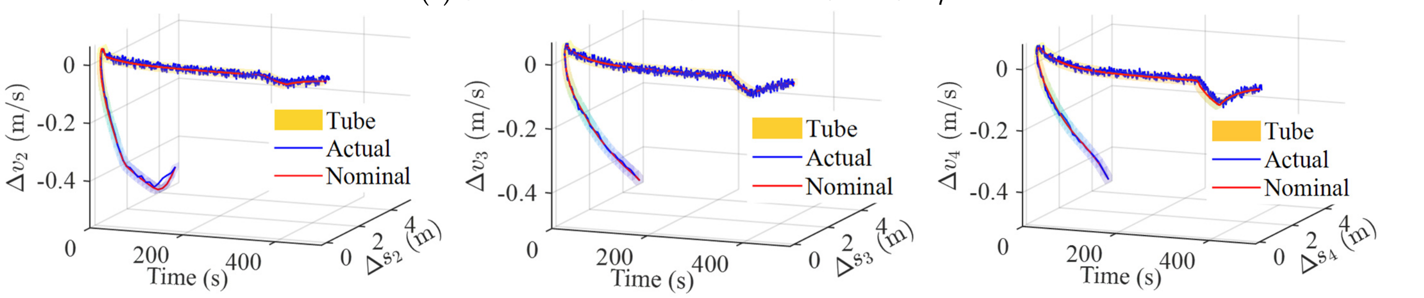

(**b**) Under the actual disturbance bound of 1.5η

Figure 7. Actual and nominal operation trajectories relative to the error Tube under wet rail-surface conditions.

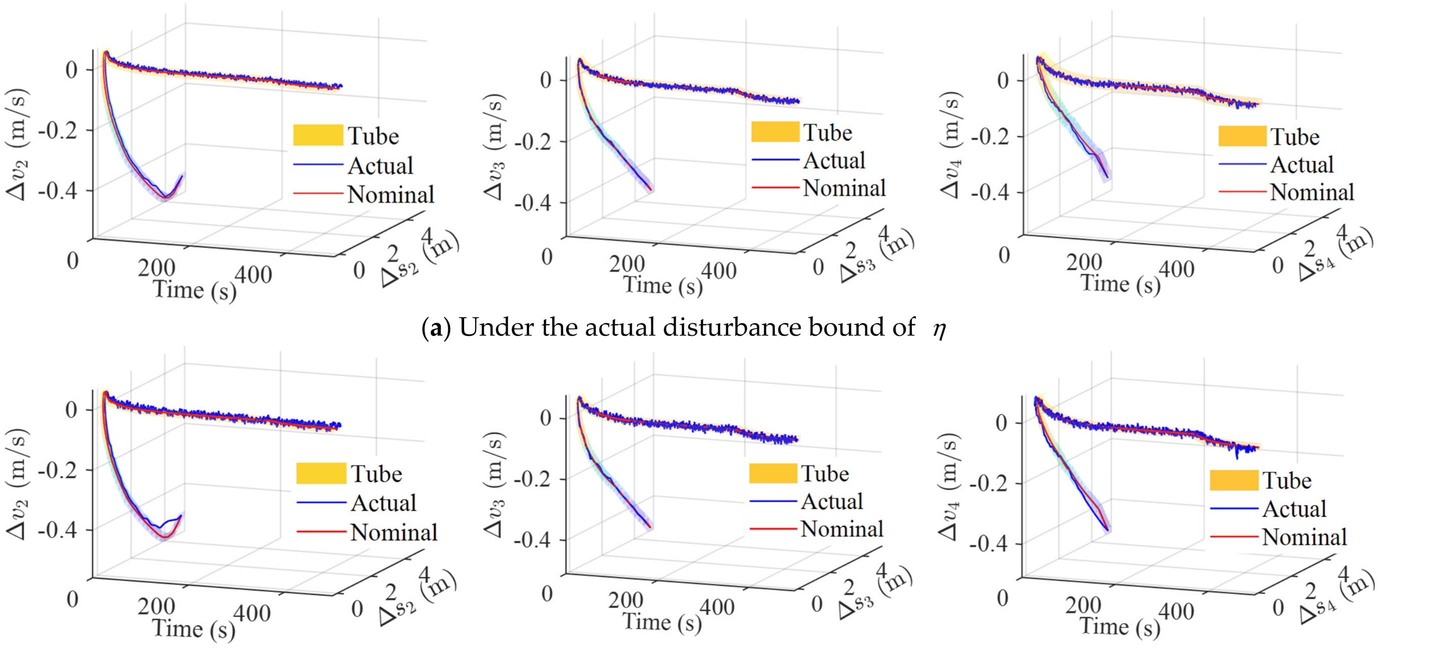

(**a**) Under the actual disturbance bound of η

(**b**) Under the actual disturbance bound of 1.5 η

Figure 8. Actual and nominal operation trajectories relative to the error Tube under rainy or snowy rail-surface conditions.

As shown in Table 4, Tube violations occur under all three rail-surface conditions. when the actual disturbance bound increases from η to 1.5η. Specifically, the speed Tube violation rates of the following trains range from 15.82% to 19.46%, and the maximum speed Tube ratios range from 1.95 to 4.57, indicating that disturbances exceeding the design disturbance bound have a significant impact on the speed state. Spacing Tube violations occur only in some trains and operation conditions, among which Train-3 under the dry rail-surface condition exhibits the highest Spacing Tube violation rate of 13.22%; Train-4 under the rainy or snowy rail-surface conditions exhibits the maximum speed Tube ratio of 4.57, which is the largest value among all operation conditions.

Figure 9 presents the speed-position-time trajectories of the HHGTs when both the design and actual disturbance bounds are set to η. The speeds of the following trains rapidly converge to that of the leader train and maintain stable tracking during subsequent operation, thereby satisfying the speed-consensus requirement specified in Equation (30). This confirms that, when the actual disturbance does not exceed the design disturbance bound, the proposed method can maintain the coordinated operation of the HHGTs.

Table 4. Tube violation statistics when the actual disturbance bound is 1.5 times the design disturbance bound.

Rail-Surface Condition	Following Train	Spacing Tube Violation Rate (%)	Speed Tube Violation Rate (%)	Maximum Spacing Tube Ratio	Maximum Speed Tube Ratio
	Train 2	0	19.25	0.58	2.06
Dry	Train 3	13.22	17.07	1.25	2.59
	Train 4	0	18.52	0.84	2.29
	Train 2	0	19.25	0.82	1.96
Wet	Train 3	0	15.82	0.45	1.95
	Train 4	0.62	16.65	1.09	2.07

	Train 2	0.62	19.46	1.12	1.98
Rainy or snowy	Train 3	0	15.82	0.51	1.97
	Train 4	5.31	17.79	1.30	4.57

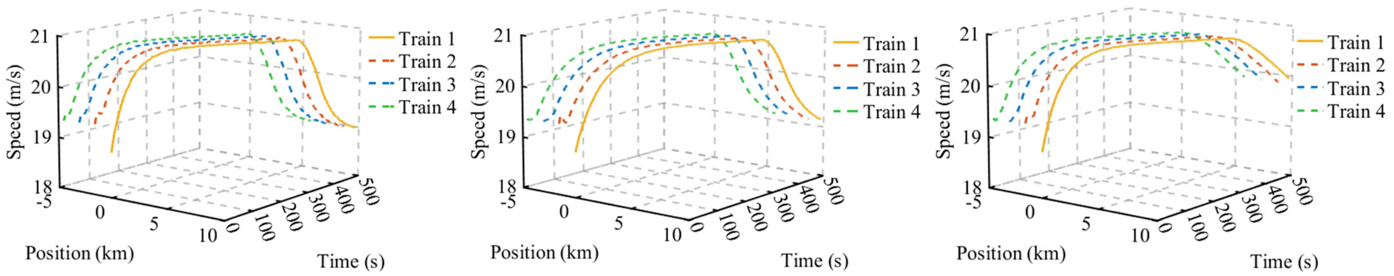

(**a**) (**b**) (**c**)

Figure 9. Speed–position–time trajectories of group trains. (**a**) Under dry rail-surface conditions. (**b**) Under wet rail-surface conditions. (**c**) Under rainy or snowy rail-surface conditions.

When the actual disturbance remains within the designed disturbance bound, the proposed Tube-based controller guarantees constraint satisfaction by confining the state deviations within the finite-horizon error Tube. When the disturbance exceeds the assumed bound, limited Tube violations may occur because the predefined bounded-disturbance assumption is no longer satisfied. Therefore, in practical applications, the disturbance bound should be selected according to the expected variation range of wheel–rail adhesion, with a suitable uncertainty margin reserved. It should be emphasized that the 1.5η case is considered only to investigate the closed-loop behavior under disturbance bound mismatch and does not imply strict theoretical robustness guarantees at this disturbance level.

4.3. Comparison with PID and Standard MPC

To evaluate the control performance of the proposed adhesion-dependent method, standard MPC and PID, which are commonly used in railway applications, are selected as benchmark controllers. Simulation studies are conducted under dry, wet, and rainy or snowy rail-surface conditions. All three control methods are evaluated using identical disturbance sequences and the same physical constraints on the control inputs. For the PID controller, the gains are set to $K_p = 0.02$, $K_i = 0.0003$, and $K_d = 0.35$, respectively. These parameters were selected through repeated simulations, and the PID output was constrained to $[-0.1, 0.1]$ $\mathrm{m/s^2}$ to satisfy the actuator constraints. Moreover, the standard MPC adopts the same sampling time, prediction horizon, and weighting matrices as the proposed adhesion-dependent Tube-MPC.

Figures 10–12 present the speed errors and spacing errors between train units obtained using PID, standard MPC, and the proposed method under the three rail-surface conditions. As shown in these figures, all three methods can reduce the initial state deviations. However, noticeable differences are observed in the peak errors and the fluctuation ranges during the stable operation phase. In general, PID produces relatively large speed and spacing errors. Standard MPC improves the control performance to some extent, whereas the proposed method achieves smaller peak errors and narrower fluctuation ranges during stable operation.

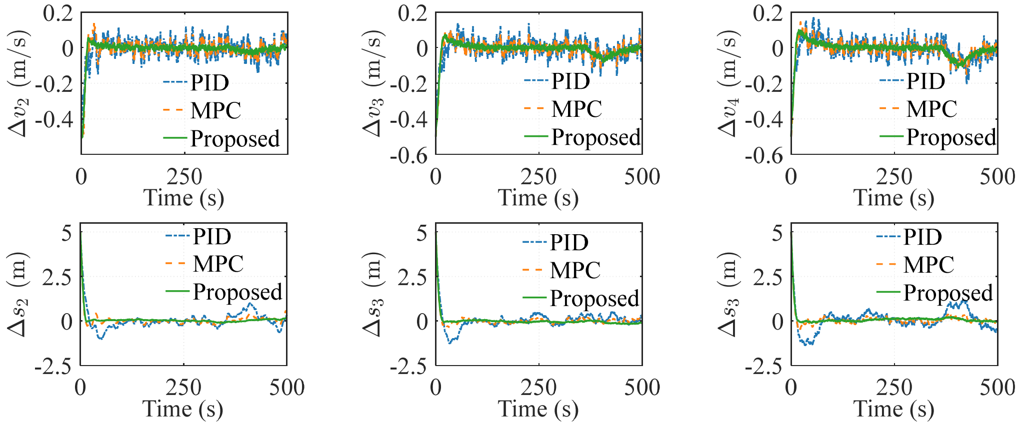

(**a**) Train 1–Train 2 (**b**) Train 1–Train 3 (**c**) Train 1–Train 4

Figure 10. Speed errors and spacing errors between train units under different control methods on dry rail-surface conditions.

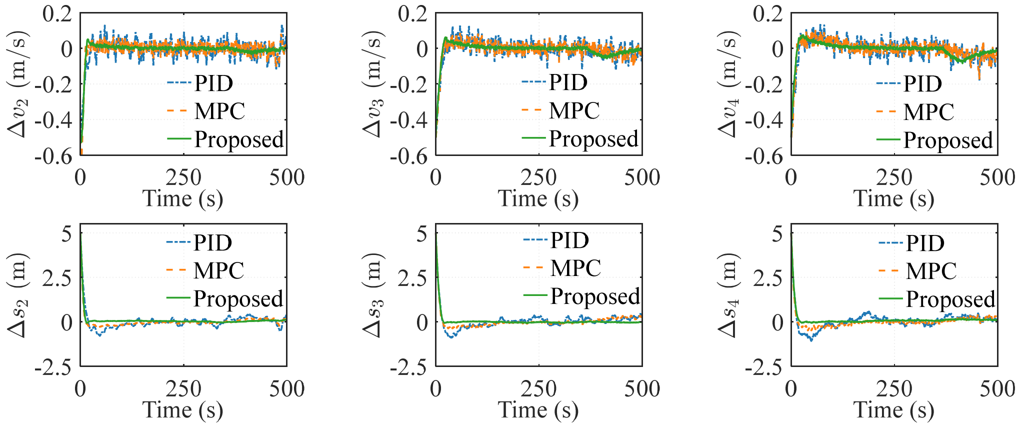

(**a**) Train 1–Train 2 (**b**) Train 1–Train 3 (**c**) Train 1–Train 4

Figure 11. Speed errors and spacing errors between train units under different control methods on wet rail-surface conditions.

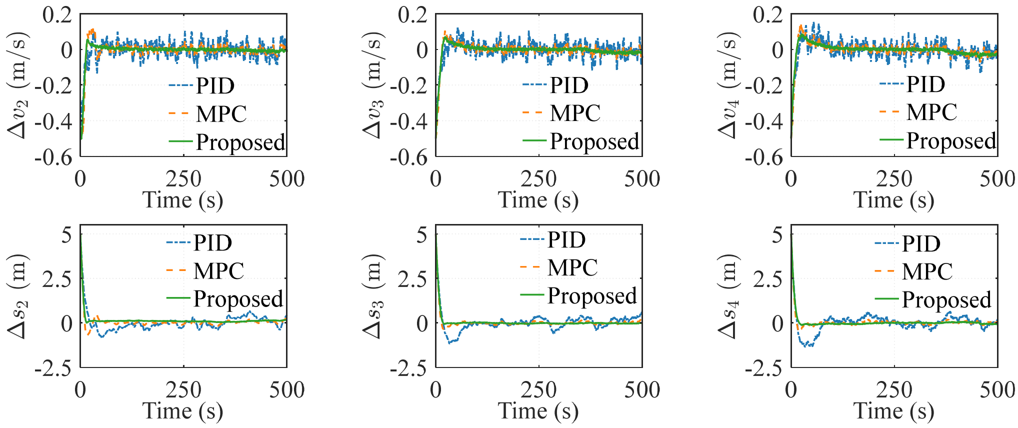

(**a**) Train 1–Train 2 (**b**) Train 1–Train 3 (**c**) Train 1–Train 4

Figure 12. Speed errors and spacing errors between train units under different control methods on rainy or snowy rail-surface conditions.

The corresponding maximum and mean speed and spacing errors are summarized in Table 5. For the adjacent-train errors, the proposed method reduces the maximum speed error by 67.19–74.13% compared with PID and by 58.84–67.12% compared with standard MPC across the three adhesion conditions. The corresponding reductions in the maximum spacing error are 72.69–83.28% and 51.84–68.35%, respectively. Similar improvements are observed for the leader-referenced errors. In particular, the proposed method limits the maximum leader-referenced speed errors to 0.0844–0.1130 m/s and the maximum spacing errors to 0.1734–0.2299 m, while the corresponding mean speed and spacing errors remain within 0.0105–0.0163 m/s and 0.0448–0.0601 m, respectively. These values are consistently lower than those obtained using PID and standard MPC.

Table 5. Tracking error comparison under different adhesion conditions.

Rail-Surface Condition	Control Method	Error Type	Maximum Speed Error (m/s)	Mean Speed Error (m/s)	Maximum Spacing Error (m)	Mean Spacing Error (m)
Dry	PID	Leader-referenced	0.2053	0.0404	1.3847	0.2907
		Adjacent-train	0.1731	0.0407	1.0756	0.2816
	MPC	Leader-referenced	0.1508	0.0294	0.5807	0.1117
		Adjacent-train	0.1380	0.0273	0.6098	0.1323
	Proposed	Leader-referenced	0.1130	0.0163	0.2299	0.0601
		Adjacent-train	0.0568	0.0109	0.2937	0.0831
Wet	PID	Leader-referenced	0.1835	0.0332	1.0909	0.2100
		Adjacent-train	0.1464	0.0335	0.7900	0.1816
	MPC	Leader-referenced	0.1795	0.0250	0.4952	0.1303
		Adjacent-train	0.1252	0.0215	0.4368	0.0695
	Proposed	Leader-referenced	0.0844	0.0141	0.1734	0.0448
		Adjacent-train	0.0412	0.0082	0.1766	0.0605
Rainy or snowy	PID	Leader-referenced	0.1534	0.0327	1.3470	0.2572
		Adjacent-train	0.1488	0.0344	1.1277	0.2642
	MPC	Leader-referenced	0.1531	0.0187	0.5955	0.0674
		Adjacent-train	0.1171	0.0166	0.5955	0.0786
	Proposed	Leader-referenced	0.0854	0.0105	0.1856	0.0535
		Adjacent-train	0.0385	0.0064	0.1885	0.0872

As shown in Table 6, the mean solution time of the proposed Tube-MPC increases from 0.8117 s to 0.9119 s at the single-train level and from 2.4348 s to 2.7356 s at the train-group level compared with standard MPC, corresponding to an increase of approximately 12.3% in both cases. Although the proposed method requires slightly higher computational effort, it achieves lower speed- and spacing-tracking errors. This indicates that the proposed Tube-MPC improves robustness and tracking performance with only a moderate increase in computational burden.

Table 6. Computational-time comparison between standard MPC and the proposed Tube-MPC.

Controller	Level	Minimum Solve Time (s)	Maximum Solve Time (s)	Mean Solve Time (s)
Standard MPC	Single train	0.2085	1.5430	0.8117
Standard MPC	Train group	0.6298	4.3914	2.4348
Proposed Tube-MPC	Single train	0.3914	1.3528	0.9119
Proposed Tube-MPC	Train group	1.1745	4.0473	2.7356

To further evaluate the control inputs of the proposed controller, Table 7 summarizes the maximum traction force and braking-force magnitude. The adhesion force for dry, wet, and rainy or snowy rail-surface are 524.73, 293.92, and 173.11 kN, respectively; all control inputs satisfy the corresponding limits, with no actuator-constraint violations.

Table 7. Maximum traction and braking force using the proposed method.

Rail-Surface Condition	Maximum Traction Force (kN)	Maximum Braking Force (kN)
Dry	330.44	290.44
Wet	293.92	278.02
Rainy or snowy	173.11	173.11

In addition, the minimum actual spacing between adjacent train units remains no less than 818.7 m, confirming that the prescribed inter-train safety spacing is maintained under all considered rail-surface conditions.

Overall, the results demonstrate that the proposed method improves both local coordination between adjacent trains and global leader-following performance. This improvement is mainly attributed to the adhesion-dependent Tube adjustment and feedback correction, which explicitly account for adhesion-induced uncertainty and thereby reduce speed and spacing deviations under different wheel–rail adhesion conditions.

5. Conclusions

This paper develops an adhesion-dependent cooperative control method for heavy-haul group trains (HHGTs) within a Tube-based model predictive control (Tube-MPC) framework. First, the control-oriented longitudinal model is formulated while retaining the position-dependent gradient resistance. Second, the effects of wheel–rail adhesion are incorporated through adhesion-dependent traction/braking constraints and a bounded equivalent acceleration disturbance derived from the force mismatch caused by adhesion saturation. Furthermore, an ancillary feedback controller, a finite-horizon bounded error Tube, and tightened nominal constraints are combined to regulate train speed and inter-train spacing. Simulation results under dry, wet, and rainy or snowy rail-surface conditions show that the trajectories of all following trains remain within the prescribed the finite-horizon error Tube over the considered prediction horizon when the actual disturbance remains within the design disturbance bound. For adjacent-train tracking, the maximum speed and spacing errors are reduced by up to 74.13% and 83.28%, respectively, relative to PID. For leader-referenced tracking, the corresponding maximum reductions reach 54.01% and 86.22%, respectively. Compared with standard MPC, the proposed method achieves improved robustness and tracking performance with a moderate increase in computational burden. These results demonstrate the effectiveness of the proposed adhesion-dependent Tube-MPC for cooperative operation of HHGTs. Future work will focus on developing a detailed multi-vehicle longitudinal dynamics model for evaluating and constraining in-train forces under complex track conditions and severe operating scenarios. Online wheel–rail adhesion estimation, adaptive disturbance bound updating, rapidly varying adhesion conditions, and distributed robust cooperative control under communication delays and packet losses will also be investigated to improve the operation reliability of HHGTs in practical environments.

Author Contributions: Conceptualization, H.Y.; methodology, H.Y. and W.Z.; software, W.Z.; validation, W.Z. and R.A.; formal analysis, H.Y.; investigation, H.Y., W.Z. and R.A.; resources, P.X., and A.L.; writing—original draft preparation, H.Y. and W.Z.; writing—review and editing, H.Y., W.Z., A.D., R.A., P.X., and A.L.; supervision, H.Y. and A.D. All authors have read and agreed to the published version of the manuscript.

Funding: This research was supported by the Natural Science Foundation of Gansu Province, China, under Grant No. 25JRRA223; the Joint Innovation Fund Project of Lanzhou Jiaotong University and

Corresponding Supporting University, China, under Grant No. LH2025020; and the Tianyou Postdoctoral Science Foundation of Lanzhou Jiaotong University, China, under Grant No. LJTYBH-2026033.

Data Availability Statement: The original contributions presented in this study are included in the article. Further inquiries can be directed to the corresponding author.

Conflicts of Interest: The authors declare that they have no conflicts of interest.

Appendix A

Proof of Theorem 1. From the disturbance error state equation $\tilde{x}_i(t_{k+1}) = A\tilde{x}_i(t_k) + B\tilde{u}_i^{vc}(t_k) + W_i(t_k)$, the speed error dynamics can be expressed as

$$\tilde{v}_i(t_{k+1}) = (1+h\delta)\tilde{v}_i(t_k) - \delta\tilde{u}_i^{vc}(t_k) - w_i(t_k)\delta \tag{A1}$$

where $\tilde{v}_i(t_k) = v_i(t_k) - \overline{v}_i(t_k)$, substituting the feedback law $\tilde{u}_i^{vc}(t_k) = k_{tube}\tilde{v}_i(t_k)$ into Equation (31):

$$\tilde{v}_i(t_{k+1}) = [1+(h-k_{tube})\delta]\tilde{v}_i(t_k) - \delta w_i(t_k) \tag{A2}$$

Define $\begin{cases} \alpha \triangleq 1+(h-k_{tube})\delta \\ \beta_k \triangleq -\delta w_i(t_k) \end{cases}$, then, $\tilde{v}_i(t_{k+1}) = \alpha\tilde{v}_i(t_k) + \beta_k$.

$$\begin{aligned}
&\tilde{v}_i(t_k) = \alpha\tilde{v}_i(t_{k-1}) + \beta_{k-1} \\
&k=1 \quad \tilde{v}_i(t_1) = \alpha\tilde{v}_i(t_0) + \beta_0 \\
&k=2 \quad \tilde{v}_i(t_2) = \alpha\tilde{v}_i(t_1) + \beta_1 = \alpha(\alpha\tilde{v}_i(t_0) + \beta_0) + \beta_1 = \alpha^2\tilde{v}_i(t_0) + \alpha\beta_0 + \beta_1 \\
&k=3 \quad \tilde{v}_i(t_3) = \alpha\tilde{v}_i(t_2) + \beta_2 = \alpha^3\tilde{v}_i(t_0) + \alpha^2\beta_0 + \alpha\beta_1 + \beta_2 \\
&\quad \vdots \\
&k \quad \tilde{v}_i(t_k) = \alpha^k\tilde{v}_i(t_0) + \sum_{m=0}^{k-1}\alpha^m\beta_{k-1-m} = [1+(h-k_{tube})\delta]^k\,\tilde{v}_i(t_0) - \sum_{m=0}^{k-1}[1+(h-k_{tube})\delta]^m\,\delta w_i(t_{k-1-m})
\end{aligned} \tag{A3}$$

By the triangle inequality $|a+b| \le |a| + |b|$, it can be obtained that

$$|\tilde{v}_i(t_k)| \le \left|[1+(h-k_{tube})\delta]^k\,\tilde{v}_i(t_0)\right| + \left|-\sum_{m=0}^{k-1}[1+(h-k_{tube})\delta]^m\,\delta w_i(t_{k-1-m})\right| \tag{A4}$$

According to Theorem 1, the initial speed prediction error satisfies $|\tilde{v}_i(t_0)| \le \dfrac{\eta}{k_{tube}-h}$, and the disturbance is bounded as $\|w_i(t)\|_\infty \le \eta$, k_{tube} is selected such that $0 \le 1+(h-k_{tube})\delta < 1$; therefore,

$$|\tilde{v}_i(t_k)| \le \frac{\eta}{k_{tube}-h}\left|[1+(h-k_{tube})\delta]^k\right| + \eta\delta\left|\sum_{m=0}^{k-1}[1+(h-k_{tube})\delta]^m\right| \tag{A5}$$

$$\begin{aligned}
|\tilde{v}_i(t_k)| &\le \frac{\eta}{k_{tube}-h}[1+(h-k_{tube})\delta]^k + \eta\frac{[1+(h-k_{tube})\delta]^k - 1}{h-k_{tube}} \\
&= \frac{\eta}{k_{tube}-h}, \quad k = 0,1,\ldots,n_p
\end{aligned} \tag{A6}$$

Therefore, Equation (A6) provides a finite-horizon pointwise bound for the speed prediction error. That is, the speed error bound $\dfrac{\eta}{k_{tube}-h}$ holds at every prediction step $k = 0,1,\ldots,n_p$.

The resulting closed-loop error dynamics are given by

$$\tilde{x}_i(t_{k+1}) = (A+BK_{tube})\tilde{x}_i(t_k) + W_i(t_k) \tag{A7}$$

To ensure that the speed error subsystem is Input-to-State Stable (ISS) with respect to the bounded disturbance, the eigenvalues associated with speed error dynamics is required to satisfy $0 \le 1 + (h - k_{tube})\delta < 1$, $k_{tube} \in \left(h, \dfrac{1}{\delta} + h\right)$. The complete closed-loop error matrix has one additional eigenvalue equal to 1, which corresponds to the spacing-integration channel. Hence, the speed error subsystem is ISS, whereas the spacing-error channel is marginally stable.

It should be emphasized that Equation (A8) is only used to characterize the asymptotic ISS property of the speed error subsystem. The subsequent finite-horizon spacing error derivation is based on the pointwise speed error bound in Equation (A6).

$$\lim_{t_k \to \infty} \left| \tilde{v}_i(t_k) \right| \le \frac{\eta}{k_{tube} - h} \tag{A8}$$

Similarly, $\tilde{s}_i(t_{k+1}) = \tilde{s}_i(t_k) + \delta \tilde{v}_i(t_k)$.

$$\begin{aligned}
&\tilde{s}_i(t_k) = \tilde{s}_i(t_{k-1}) + \delta \tilde{v}_i(t_{k-1}) \\
&k = 1 \quad \tilde{s}_i(t_1) = \tilde{s}_i(t_0) + \delta \tilde{v}_i(t_0) \\
&k = 2 \quad \tilde{s}_i(t_2) = \tilde{s}_i(t_1) + \delta \tilde{v}_i(t_1) = \tilde{s}_i(t_0) + \delta \tilde{v}_i(t_0) + \delta \tilde{v}_i(t_1) \\
&\quad \vdots \\
&k = k \quad \tilde{s}_i(t_k) = \tilde{s}_i(t_0) + \delta \tilde{v}_i(t_0) + \delta \tilde{v}_i(t_1) + \delta \tilde{v}_i(t_2) + \cdots + \delta \tilde{v}_i(t_{k-1})
\end{aligned} \tag{A9}$$

Therefore, $\left| \tilde{s}_i(t_k) \right| = \left| \tilde{s}_i(t_0) + \sum_{m=0}^{k-1} \tilde{v}_i(t_m)\delta \right|$, assuming that the spacing error is zero at the initial time, $\tilde{s}_i(t_0) = 0$, the maximum spacing error occurs at $k = n_p$ within the prediction horizon, i.e.,

$$\left| \tilde{s}_i(t_k) \right| = \left| \sum_{m=0}^{k-1} \tilde{v}_i(t_m)\delta \right| \le \frac{\eta \delta k}{k_{tube} - h} = \frac{\eta \delta n_p}{k_{tube} - h} \tag{A10}$$

Therefore, the spacing error is the discrete-time accumulation of the speed prediction error. Although the spacing channel is marginally stable because of the unit eigenvalue, its error remains explicitly bounded over the finite prediction horizon. The maximum conservative spacing error bound is reached by setting $k = n_p$.

Therefore, the above analysis establishes the input-to-state stability of the speed error subsystem and the finite-horizon boundedness of the spacing error. Accordingly, the set $\tilde{\mathbb{X}}$ is interpreted as a finite-horizon bounded error Tube.

Based on the preceding analysis, the proof of Theorem 1 is complete. □

Proof of Theorem 2. According to the control law given in (31), the tightened constraint of the nominal control input $\bar{u}_i^{vc}$ in (23) can be derived by combining the original input constraint in (33) with the finite-horizon bounded error Tube constraint in (32). The relationship among the sets $\mathbb{U}$, $\bar{\mathbb{U}}$, and $\tilde{\mathbb{X}}$ ensures that, for any error state satisfying $\tilde{x}_i \in \tilde{\mathbb{X}}$, the actual control input u_i^{vc} remains within the original admissible input set $\mathbb{U}$ if the nominal control input satisfies $\bar{u}_i^{vc} \in \bar{\mathbb{U}}$. Therefore, the proposed constraint-tightening strategy guarantees robust satisfaction of the input constraints over the considered finite prediction horizon, provided that the actual disturbance remains within the design disturbance bound.

By substituting the state-variable constraints in Equation (28) and the finite-horizon bounded error Tube in Equation (32) into $\bar{\mathbb{X}} \triangleq \mathbb{X} \ominus \tilde{\mathbb{X}}$, the tightened constraint set for the nominal state variable $\bar{x}_i$, as given in Equation (34), can be obtained. According to the relationship among the actual state, the nominal state, and the error state, $x_i = \bar{x}_i + \tilde{x}_i$, when $\bar{x}_i \in \bar{\mathbb{X}}$, $\tilde{x}_i \in \tilde{\mathbb{X}}$, it follows that $x_i = \bar{x}_i + \tilde{x}_i \in \mathbb{X}$. Therefore, as long as the nominal state satisfies the tightened state constraints and the disturbance state is always confined within the finite-horizon bounded error Tube, the actual state necessarily satisfies the original state constraints. Furthermore, by replacing the general nominal state $\bar{x}_i$ with the optimal nominal solution $\bar{x}_{i,o}$ obtained from the optimization problem, we obtain $x_i \in \bar{x}_{i,o} \oplus \tilde{\mathbb{X}}$.

This indicates that the actual state trajectory always remains within a Tube centered on the optimal nominal trajectory, with the finite-horizon bounded error Tube $\tilde{\mathbb{X}}$ as its cross-section. Therefore, the proposed constraint-tightening strategy ensures that the group train system (9) continues to satisfy the original state constraints under bounded disturbances.

The proof of Theorem 2 is complete. □

Proof of Theorem 3. At time t_k, construct a feasible control sequence $\bar{u}_{i,e}^{vc}(\cdot \mid t_k)$ as

$$\bar{u}_{i,e}^{vc}(t_{k+m} \mid t_k) = \begin{cases} \bar{u}_{i,o}^{vc}(t_{k+m+1} \mid t_{k-1}) & m = 0,1,\ldots,n_p - 2 \\ K_f \bar{x}_i(t_{k+n_p-1} \mid t_k) + \dfrac{d_{i,2}(t_k)}{\delta} & m = n_p - 1 \end{cases} \tag{A11}$$

where the $n_p - 1$ control inputs are obtained by shifting forward the optimal control sequence at time t_{k-1}, while the last control input is generated by the terminal feedback controller.

Based on the above feasible control sequence, a feasible predicted state trajectory at time t_k can be constructed as

$$\bar{x}_{i,e}(t_{k+m} \mid t_k) = \begin{cases} \bar{x}_{i,o}(t_{k+m+1} \mid t_{k-1}) & m = 0,1,\ldots n_p - 1 \\ A\bar{x}_{i,e}(t_{k+n_p-1} \mid t_k) + B\bar{u}_{i,e}^{vc}(t_{k+n_p-1} \mid t_k) + D_i(t_k) & m = n_p \end{cases} \tag{A12}$$

Since the first $n_p - 1$ predicted states are obtained by shifting forward the optimal state trajectory from the previous time instant, it follows that $\bar{x}_{i,e}(t_{k+m} \mid t_k) \in \bar{\mathbb{X}}$ and $\bar{u}_i^{vc}(t_{k+m} \mid t_k) \in \bar{\mathbb{U}}$ are both satisfied. Therefore, it remains only to prove that the terminal state satisfies the terminal constraint.

Under the terminal steady-cruise condition, the leader train operates at an approximately constant speed. Accordingly, its control acceleration is close to zero, $u_1^{vc} \approx 0$. Moreover, since $h_i = -\dfrac{1}{M_i}(c_1 + 2c_2 v_r)$, the large mass of a heavy-haul train makes h_i very small. Therefore, over the terminal interval, $u_1^{vc} + hv_1 \approx 0$. Hence, the first component of D_i, $d_{i,1}(t) = -\delta(i-1)t_d(u_1^{vc} + hv_1)$, can be taken as zero under the terminal steady-cruise approximation. Thus, the terminal value of D_i is written as $D_i(t_k) = \begin{bmatrix} 0 \\ d_{i,2}(t_k) \end{bmatrix}$.

By substituting the terminal controller $\bar{u}_f(t_k) = K_f \bar{x}_i(t_k) + \dfrac{d_{i,2}(t_k)}{\delta}$ into the system model, the terminal state transition equation can be obtained as

$$\bar{x}_i(t_{k+n_p} \mid t_k) = A\bar{x}_i(t_{k-1+n_p} \mid t_{k-1}) + B\bar{u}_f(t_{k-1+n_p} \mid t_k) + D_i(t_{k-1+n_p} \mid t_{k-1}) \tag{A13}$$

Since $B = \begin{pmatrix} 0 \\ -\delta \end{pmatrix}$, it follows that $B\dfrac{d_{i,2}}{\delta} = \begin{pmatrix} 0 \\ -d_{i,2} \end{pmatrix}$, and therefore

$$B\frac{d_{i,2}}{\delta} + D_i = \begin{pmatrix} 0 \\ -d_{i,2} \end{pmatrix} + \begin{pmatrix} 0 \\ d_{i,2} \end{pmatrix} = 0 \tag{A14}$$

Consequently, the terminal state transition becomes

$$\bar{x}_i(t_{k+n_p} \mid t_k) = A_f \bar{x}_i(t_{k-1+n_p} \mid t_{k-1}) \tag{A15}$$

where $A_f = A + BK_f$.

To ensure that the terminal state gradually converges to the equilibrium point, the closed-loop matrix A_f is required to have eigenvalues with magnitudes less than 1. According to the discrete-time Linear Quadratic Regulator (LQR) theory, the terminal feedback gain is selected as $\mathrm{K}_f = -(R + \mathrm{B}^{\mathrm{T}}\mathrm{PB})^{-1}\mathrm{B}^{\mathrm{T}}\mathrm{PA}$, which ensures that A_f satisfies the stability condition [37].

Furthermore, the terminal constraint set $\mathbb{X}_f$ is designed as a disturbance-dependent bounded error set with respect to A_f, i.e.,
if

$$\overline{x}_i(t_{k+n_p-1} \mid t_{k-1}) \in \mathbb{X}_f \tag{A16}$$

then

$$\mathrm{K}_f \overline{x}_i(t_{k+n_p-1} \mid t_{k-1}) + \frac{d_{i,2}(t_k)}{\delta} \in \overline{\mathbb{U}} \tag{A17}$$

and

$$A_f \overline{x}_i(t_{k+n_p-1} \mid t_{k-1}) \in \mathbb{X}_f \tag{A18}$$

Therefore, $\overline{x}_i(t_{k+n_p} \mid t_k) \in \mathbb{X}_f$, which means that the terminal state remains within the terminal constraint set under the action of the terminal controller.

Consequently, it can be proven that if the Tube-MPC optimization problem is feasible at time t_{k-1}, then by recursive induction, it is also feasible at time t_k. Based on the preceding analysis, the proof of Theorem 3 is complete. □

Proof of Theorem 4. According to the feasible control sequence in Equation (A11) and the predicted state trajectory in Equation (A12), the suboptimal cost at time t_k, $J_i(\overline{x}_{i,e}(t_k), \overline{u}_{i,e}^{vc}(t_k), \overline{x}_{i-1,e}(t_k))$, can be calculated and compared with the optimal cost. The optimal cost is selected as the Lyapunov function of the closed-loop HHGTs system:

$$V(t_k) = J_i(\overline{x}_{i,o}(t_k), \overline{u}_{i,o}^{vc}(t_k), \overline{x}_{i-1,e}(t_k)) \tag{A19}$$

Therefore, it is sufficient to prove that $V(t_k) < J_i(\overline{x}_{i,e}(t_k), \overline{u}_{i,e}^{vc}(t_k), \overline{x}_{i-1,e}(t_k)) < V(t_{k-1})$ holds in order to establish the stability of the closed-loop system.

According to the objective function in Equation (38) and the triangle inequality, the following result can be derived:

$$\begin{aligned}
&V(t_k) - V(t_{k-1}) < \Delta J_i \\
&= J_i(t_k) - J_i(t_{k-1}) \\
&= \sum_{m=0}^{n_p-1} L_i\left(\overline{x}_{i,e}(t_{k+m} \mid t_k), \overline{u}_{i,e}^{vc}(t_{k+m} \mid t_k), \overline{x}_{i-1,e}(t_{k+m} \mid t_k)\right) + G_i\left(\overline{x}_{i,e}(t_{k+n_p} \mid t_k), \overline{x}_{i-1,e}(t_{k+n_p} \mid t_k)\right) \\
&\quad - \sum_{m=0}^{n_p-1} L_i\left(\overline{x}_{i,o}(t_{k-1+m} \mid t_{k-1}), \overline{u}_{i,o}^{vc}(t_{k-1+m} \mid t_{k-1}), \overline{x}_{i-1,e}(t_{k-1+m} \mid t_{k-1})\right) \\
&\quad - G_i\left(\overline{x}_{i,o}(t_{k-1+n_p} \mid t_{k-1}), \overline{x}_{i-1,e}(t_{k-1+n_p} \mid t_{k-1})\right) \\
&= -L_i\left(\overline{x}_{i,o}(t_{k-1} \mid t_{k-1}), \overline{u}_{i,o}^{vc}(t_{k-1} \mid t_{k-1}), \overline{x}_{i-1,e}(t_{k-1} \mid t_{k-1})\right) \\
&\quad + L_i\left(\overline{x}_{i,e}(t_{k+n_p-1} \mid t_k), \overline{u}_{i,e}^{vc}(t_{k+n_p-1} \mid t_k), \overline{x}_{i-1,e}(t_{k+n_p-1} \mid t_k)\right) \\
&\quad + G_i\left(\overline{x}_{i,e}(t_{k+n_p} \mid t_k), \overline{x}_{i-1,e}(t_{k+n_p} \mid t_k)\right) - G_i\left(\overline{x}_{i,o}(t_{k-1+n_p} \mid t_{k-1}), \overline{x}_{i-1,e}(t_{k-1+n_p} \mid t_{k-1})\right) \\
&= -L_i\left(\overline{x}_{i,o}(t_{k-1} \mid t_{k-1}), \overline{u}_{i,o}^{vc}(t_{k-1} \mid t_{k-1}), \overline{x}_{i-1,e}(t_{k-1} \mid t_{k-1})\right) \\
&\quad + \left\| Q\overline{x}_{i,e}(t_{k+n_p-1} \mid t_k) \right\|_2 + \left\| F\left(\overline{x}_{i,e}(t_{k+n_p-1} \mid t_k) - \overline{x}_{i-1,e}(t_{k+n_p-1} \mid t_k)\right) \right\|_2 + \left\| R\overline{u}_{i,e}^{vc}(t_{k+n_p-1} \mid t_k) \right\|_2 \\
&\quad + \left\| P\overline{x}_{i,e}(t_{k+n_p} \mid t_k) \right\|_2 - \left\| P\overline{x}_{i,o}(t_{k-1+n_p} \mid t_{k-1}) \right\|_2 + \left\| P\left(\overline{x}_{i,e}(t_{k+n_p} \mid t_k) - \overline{x}_{i-1,e}(t_{k+n_p} \mid t_k)\right) \right\|_2 \\
&\quad - \left\| P\left(\overline{x}_{i,o}(t_{k-1+n_p} \mid t_{k-1}) - \overline{x}_{i-1,e}(t_{k-1+n_p} \mid t_{k-1})\right) \right\|_2
\end{aligned} \tag{A20}$$

Let

$$\begin{aligned}
z_i &= \overline{x}_{i,o}(t_{k+n_p-1} \mid t_{k-1}) \\
z_{i-1} &= \overline{x}_{i-1,e}(t_{k+n_p-1} \mid t_{k-1}) \\
e_i &= z_i - z_{i-1}
\end{aligned} \tag{A21}$$

Since the first $n_p - 1$ control inputs are consistent with the optimal sequence at the previous time instant,

$$\begin{aligned} &\bar{x}_{i,e}(t_{k+n_p-1} \mid t_k) = \bar{x}_{i,o}(t_{k+n_p-1} \mid t_{k-1}) = z_i \\ &\bar{x}_{i-1,e}(t_{k+n_p-1} \mid t_k) = z_{i-1} \end{aligned} \tag{A22}$$

Since $A_f = A + B\mathrm{K}_f$, then

$$\begin{aligned} &\bar{x}_{i,e}(t_{k+n_p} \mid t_k) = A_f z_i \\ &\bar{x}_{i-1,e}(t_{k+n_p} \mid t_k) = A_f z_{i-1} \\ &\bar{x}_{i,e}(t_{k+n_p} \mid t_k) - \bar{x}_{i-1,e}(t_{k+n_p} \mid t_k) = A_f e_i \end{aligned} \tag{A23}$$

$$\begin{aligned} \Delta J_i &= -L_i\left(\bar{x}_{i,o}(t_{k-1} \mid t_{k-1}), \bar{u}_{i,o}^{vc}(t_{k-1} \mid t_{k-1}), \bar{x}_{i-1,e}(t_{k-1} \mid t_{k-1})\right) \\ &+ \|Qz_i\|_2 + \|Fe_i\|_2 + \|R\mathrm{K}_f z_i\|_2 \\ &+ \|PA_f z_i\|_2 - \|Pz_i\|_2 \\ &+ \|PA_f e_i\|_2 - \|Pe_i\|_2 \\ &< \left\|\left(Q + \mathrm{K}_f^T R\mathrm{K}_f + A_f^T PA_f - P\right) z_i\right\|_2 + \left\|\left(A_f^T PA_f + F - P\right) e_i\right\|_2 \end{aligned} \tag{A24}$$

$$\begin{aligned} V(t_k) - V(t_{k-1}) &= \Delta J \\ &< \left\|\left(A_f^T PA_f + Q - P + \mathrm{K}_f^T R\mathrm{K}_f\right)\bar{x}_i(t_{k-1+n_p} \mid t_{k-1})\right\|_2 \\ &+ \left\|\left(A_f^T PA_f + F - P\right)\left(\bar{x}_i(t_{k-1+n_p} \mid t_{k-1}) - \bar{x}_{i-1}(t_{k-1+n_p} \mid t_{k-1})\right)\right\|_2 \end{aligned} \tag{A25}$$

Combining the stability conditions in Equation (35), we obtain $V(t_k) - V(t_{k-1}) < 0$, which establishes the asymptotic stability of the nominal closed-loop system. Accordingly, the Lyapunov function decreases monotonically and the nominal states asymptotically converge to the cooperative equilibrium.

$$\begin{aligned} &\lim_{k\to\infty} \|\bar{x}_i(t_k)\|_2 = 0 \\ &\lim_{k\to\infty} \|\bar{x}_i(t_k) - \bar{x}_{i-1}(t_k)\|_2 = 0 \end{aligned} \tag{A26}$$

According to the relationship among the actual state, nominal state, and disturbance state, $x_i = \bar{x}_i + \tilde{x}_i$, and the finite-horizon bounded error Tube defined in Equation (32), under $\|w_i(t)\|_\infty \le \eta$, the disturbance state satisfies $\tilde{x}_i \in \tilde{\mathbb{X}}$. Hence, its norm is bounded by a finite value determined by η, namely,

$$\|\tilde{x}_i(t_k)\|_2 \le \gamma(\eta), 0 < \forall k < n_p \tag{A27}$$

Let $\gamma(\eta) = \max_{\tilde{x}_i \in \tilde{\mathbb{X}}} \|\tilde{x}_i(t_k)\|_2$, then, by the triangle inequality,

$$\begin{aligned} \|x_i(t_k)\|_2 &= \|\bar{x}_i(t_k) + \tilde{x}_i(t_k)\|_2 \\ &\le \|\bar{x}_i(t_k)\|_2 + \|\tilde{x}_i(t_k)\|_2 \\ &\le \|\bar{x}_i(t_k)\|_2 + \gamma(\eta) \\ \|x_i(t_k) - x_{i-1}(t_k)\|_2 &= \|\bar{x}_i(t_k) - \bar{x}_{i-1}(t_k) + \tilde{x}_i(t_k) - \tilde{x}_{i-1}(t_k)\|_2 \\ &\le \|\bar{x}_i(t_k) - \bar{x}_{i-1}(t_k)\|_2 + \|\tilde{x}_i(t_k)\|_2 + \|\tilde{x}_{i-1}(t_k)\|_2 \\ &\le \|\bar{x}_i(t_k) - \bar{x}_{i-1}(t_k)\|_2 + \gamma(\eta) + \gamma(\eta) \end{aligned} \tag{A28}$$

Therefore,

$$\begin{aligned} &\lim_{k\to n_p} \|x_i(t_k)\|_2 \le \gamma(\eta) \\ &\lim_{k\to n_p} \|x_i(t_k) - x_{i-1}(t_k)\|_2 \le 2\gamma(\eta) \end{aligned} \tag{A29}$$

Thus, the nominal closed-loop system is asymptotically stable, while the actual closed-loop system remains bounded over the finite prediction horizon under bounded disturbances. Therefore, the cooperative control objectives are satisfied within disturbance-dependent bounds under the proposed Tube-MPC controller. This completes the proof of Theorem 4. □

References

1. Bock, U.; Bikker, G. Design and Development of a Future Freight Train Concept—"Virtually Coupled Train Formations". *IFAC Proc. Vol.* **2000**, *33*, 395–400. https://doi.org/10.1016/S1474-6670(17)38176-4.
2. European Commission. CORDIS: EU Research Projects–Shift2Rail Projects. Available online: https://cordis.europa.eu (accessed on 20 June 2022).
3. Yu, X.; Li, W.; Li, S.; Yang, Y.; Peng, J. Cooperative Reference Velocity Regulation Control for Virtual Coupling Systems of Heavy-Haul Trains. *Sustainability* **2023**, *15*, 13425. https://doi.org/10.3390/su151813425.
4. Terlizzi, M.; Glielmo, L.; Liuzza, D. A Safe and Robust Control System Architecture for Trains Virtual Coupling. *IEEE Trans. Control Syst. Technol.* **2026**, *34*, 829–844. https://doi.org/10.1109/TCST.2025.3649895.
5. Stanley, A.; Liu, Q.; Wu, Q. Particle swarm optimisation of a PID-based virtual coupling controller for metro railway trains. *Proc. Inst. Mech. Eng. Part F J. Rail Rapid Transit* **2025**, *239*, 679–688. https://doi.org/10.1177/09544097251343749.
6. Qiu, S.; Li, N.; Wei, X.; Li, G. Research on the stability of virtual coupling train formation based on a PID controller under the influence of time delay. *Transp. Saf. Environ.* **2024**, *6*, tdad037. https://doi.org/10.1093/tse/tdad037.
7. Park, J.; Lee, B.H.; Eun, Y. Virtual coupling of railway vehicles: Gap reference for merge and separation, robust control, and position measurement. *IEEE Trans. Intell. Transp. Syst*. **2020**, *23*, 1085–1096.
8. He, Z.; Xu, N.; Liang, K.; Gao, Z.; Zhao, X.; Sheng, Z. Disturbance Observer-Based Terminal Sliding Mode Control Approach for Virtual Coupling Train Set. *Appl. Sci.* **2026**, *16*, 887. https://doi.org/10.3390/app16020887.
9. Liu, C.; Xu, Z. Multi-Agent System Based Cooperative Control for Speed Convergence of Virtually Coupled Train Formation. *Sensors* **2024**, *24*, 4231. https://doi.org/10.3390/s24134231.
10. Wang, H.; Zhao, Q.; Lin, S.; Cui, D.; Luo, C.; Zhu, L.; Wang, X.; Tang, T. A Reinforcement Learning Empowered Cooperative Control Approach for IIoT-Based Virtually Coupled Train Sets. *IEEE Trans. Ind. Inform*. **2021**, *17*, 4935–4945. https://doi.org/10.1109/TII.2020.3024946.
11. Basile, G.; Lui, D.G.; Petrillo, A.; Santini, S. Deep Deterministic Policy Gradient Virtual Coupling Control for the Coordination and Manoeuvring of Heterogeneous Uncertain Nonlinear High-Speed Trains. *Eng. Appl. Artif. Intell*. **2024**, *133*, 108120. https://doi.org/10.1016/j.engappai.2024.108120.
12. Xun, J.; Chen, M.; Liu, Y.; Liu, F. An Overspeed Protection Mechanism for Virtual Coupling in Railway. *IEEE Access* **2020**, *8*, 187400–187410. https://doi.org/10.1109/ACCESS.2020.3029147.
13. Su, S.; She, J.; Li, K.; Wang, X.; Zhou, Y. A Nonlinear Safety Equilibrium Spacing-based Model Predictive Control for Virtually Coupled Train Set over Gradient Terrains. *IEEE Trans. Transp. Electrif.* **2021**, *8*, 2810–2824. https://doi.org/10.1109/TTE.2021.3134669.
14. Felez, J.; Kim, Y.; Borrelli, F. A Model Predictive Control Approach for Virtual Coupling in Railways. *IEEE Trans. Intell. Transp. Syst.* **2019**, *20*, 2728–2739. https://doi.org/10.1109/TITS.2019.2914910.
15. Liu, Y.; Liu, R.; Wei, C.; Xun, J.; Tang, T. Distributed Model Predictive Control Strategy for Constrained High-Speed Virtually Coupled Train Set. *IEEE Trans. Veh. Technol.* **2022**, *71*, 171–183. https://doi.org/10.1109/TVT.2021.3130715.
16. Lin, Z.; Yu, H.; Tai, G.; Guo, W.; Shi, Z.; Yu, L.; Huang, Y. Research on Virtually Coupled Train Formation Control of Heavy-Haul Train Based on Improved MPC under Moving Block System. *J. China Railw. Soc*. **2024**, *46*, 74–81. https://doi.org/10.3969/j.issn.1001-8360.2024.02.009.
17. Wang, C.; Zhan, J.; Zhang, L. Distributed Model Predictive Control for Virtually Coupled Heavy-Haul Trains. In Proceedings of the 2025 37th Chinese Control and Decision Conference (CCDC), Xiamen, China, 24–26 May 2025; pp. 4563–4568. https://doi.org/10.1109/CCDC65474.2025.11091006.
18. Wei, W.; Wang, J.; Liu, Y.; Zhou, Z. Research on Layered Control of Virtual Coupling Heavy-Haul Trains for Long Downhill Road Conditions. *J. Railw. Sci. Eng*. **2026**, *23*, 1612–1624. https://doi.org/10.19713/j.cnki.43-1423/u.T20251061.
19. Luo, X.; Tang, T.; Chai, M.; Liu, H. A Hierarchical MPC Approach for Arriving-Phase Operation of Virtually Coupled Train Set. *IEEE Trans. Intell. Transp. Syst*. **2024**, *25*, 7237–7249. https://doi.org/10.1109/TITS.2023.3347409.
20. Liu, H.; Luo, X.; Tang, T.; Zhang, Y.; Chai, M. A Hierarchical Control Approach for Virtual Coupling in Metro Trains. *Comput.-Aided Civ. Infrastruct. Eng*. **2024**, *39*, 1318–1336. https://doi.org/10.1111/mice.13138.
21. Li, Z.; Zhong, L.; Yang, H.; Zhou, L. Distributed Cooperative Tracking Control Strategy for Virtual Coupling Trains: An Event-Triggered Model Predictive Control Approach. *Processes* **2023**, *11*, 3293. https://doi.org/10.3390/pr11123293.
22. Zhu, L.; Li, X.; Huang, D.; Qin, N. Cooperative Control of Virtually Coupled Trains Considering Train-to-Train Communication Cycle: A Tube-Based Model Predictive Control Approach. *Veh. Syst. Dyn.* **2025**, *63*, 3–25. https://doi.org/10.1080/00423114.2024.2394127.

23. Luo, X.; Tang, T.; Lin, B.; Liu, H. A Robust Model Predictive Control Approach for Reducing Following Distance between Virtually Coupled Unit Trains. *J. China Railw. Soc*. **2023**, *45*, 68–76. https://doi.org/10.3969/j.issn.1001-8360.2023.08.008.
24. Mayne, D.Q.; Seron, M.M.; Raković, S.V. Robust model predictive control of constrained linear systems with bounded disturbances. *Automatica* **2005**, *41*, 219–224.
25. Luo, X.; Tang, T.; Lu, X.; Lv, J.; Liu, H. Robust Constraint Satisfaction and Stability of Virtually Coupled Train Set with Uncertain Dynamics: A Dual-Mode Robust MPC Approach. *Transp. Res. Part C Emerg. Technol.* **2023**, *156*, 104356. https://doi.org/10.1016/j.trc.2023.104356.
26. Xi, W.; Hu, M.; Wang, H.; Dong, H.; Ying, Z. Formation Control for Virtual Coupling Trains with Parametric Uncertainty and Unknown Disturbances. *IEEE Trans. Circuits Syst. II Express Briefs* **2023**, *70*, 3429–3433. https://doi.org/10.1109/TCSII.2023.3262511.
27. Wang, X.; Su, S.; Cao, Y.; Qin, L.; Liu, W. Robust Cruise Control for the Heavy-Haul Train Subject to Disturbance and Actuator Saturation. *IEEE Trans. Intell. Transp. Syst*. **2023**, *24*, 8003–8013. https://doi.org/10.1109/TITS.2023.3264238.
28. Rong, L.; Ma, S.; Wang, H.; Gong, T.; Li, Y.; Qi, X.; Ji, M. Stochastic Game-Based Anti-Jamming Control Method for Heavy-Haul Train Group Operation. *Electronics* **2025**, *14*, 4360. https://doi.org/10.3390/electronics14224360.
29. Xing, J.; Ren, Y.; Liu, R.; Wang, X.; Chang, Y.; Min, S.; Li, A.; Wang, D.; Yu, H. Robust Control Approach for Virtually Coupled Train Set with Uncertain Communication. *Transp. A Transp. Sci.* **2026**, *in press*. https://doi.org/10.1080/23249935.2026.2654744.
30. Luo, X.; Tang, T.; Yin, J.; Liu, H. A Robust MPC Approach with Controller Tuning for Close Following Operation of Virtually Coupled Train Set. *Transp. Res. Part C Emerg. Technol.* **2023**, *151*, 104116. https://doi.org/10.1016/j.trc.2023.104116.
31. Wang, X.; Song, Z.; Zhu, S.; He, Q.; Ge, X.; Wu, Q. Resilient Platoon Operation Control of Heterogeneous Heavy-Haul Trains in Complex Environments. *IEEE Trans. Intell. Veh.* **2025**, *10*, 1805–1819. https://doi.org/10.1109/TIV.2024.3435751.
32. Uyulan, C.; Gokasan, M.; Bogosyan, S. Comparison of the Re-Adhesion Control Strategies in High-Speed Train. *Proc. Inst. Mech. Eng. Part I J. Syst. Control Eng*. **2018**, *232*, 92–105. https://doi.org/10.1177/0959651817737857.
33. Hauck, M.; Schmidt, P.; Kobelski, A.; Streif, S. A Map-based Model Predictive Control Approach for Train Operation. In Proceedings of the 2023 European Control Conference (ECC), Bucharest, Romania, 13–16 June 2023; pp. 1–6. https://doi.org/10.23919/ECC57647.2023.10178135.
34. Rao, Z. *Train Traction Calculation*, 3rd ed.; China Railway Publishing House: Beijing, China, 2016.
35. Zhao, K.; Li, P.; Zhang, C.; He, J.; Li, Y.; Yin, T. Online Accurate Estimation of the Wheel-Rail Adhesion Coefficient and Optimal Adhesion Antiskid Control of Heavy-Haul Electric Locomotives Based on Asymmetric Barrier Lyapunov Function. *J. Sens.* **2018**, *2018*, 2740679. https://doi.org/10.1155/2018/2740679.
36. Liu, Y.; Zhou, Y.; Su, S.; Xun, J.; Tang, T. Control strategy for stable formation of high-speed virtually coupled trains with disturbances and delays. *Comput.-Aided Civ. Infrastruct. Eng.* **2023**, *38*, 621–639. https://doi.org/10.1111/mice.12873. Correction in *Comput.-Aided Civ. Infrastruct. Eng.* **2023**, 38, 1892.
37. Zhou, Y.; Wang, M.; Ahn, S. Distributed model predictive control approach for cooperative car-following with guaranteed local and string stability. *Transp. Res. Part B Methodological.* **2019**, *128*, 69–86. https://doi.org/10.1016/j.trb.2019.07.001.